LITHOSPHERIC DEFLECTION UNDER THE

NECKER RIDGE AND PLATE THICKNESS

DETERMINATIONS

A THESIS SUBMITTED TO THE GRADUATE DIVISION OF THE
UNIVERSITY OF HAWAII IN PARTIAL FULFILLMENT
OF THE REQUIREMENTS FOR THE DEGREE OF

MASTER OF SCIENCE
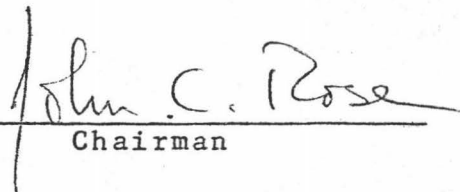
IN GEOLOGY AND GEOPHYSICS

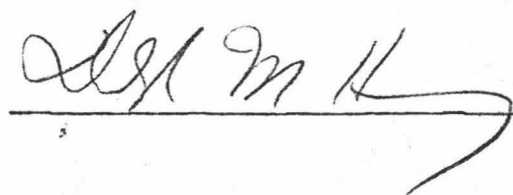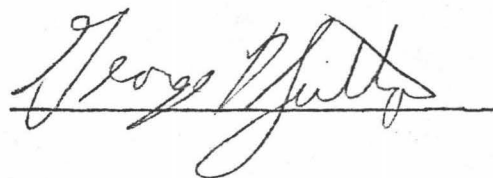APRIL 1977

By

John F. Meyer Jr.

Thesis Committee:

John C. Rose, Chairman
George H. Sutton
Donald M. Hussong

We certify that we have read this thesis and that in our opinion it is satisfactory in scope and quality as a thesis for the degree of Master of Science in Geology and Geophysics.

THESIS COMMITTEE

John C. Rose
Chairman

An abundance of new data for the Necker Ridge area
have been collected and presented in the form of bathy-
metric and free-air anomaly contour maps as well as a
series of profiles projected perpendicular to the ridge.
The sediment thickness is determined for three of these
profiles and a density profiling technique is used to de-
termine an average density for the ridge of 2.4 gm/cc.
Calculations are made of lithospheric deflections due to
loading by the Necker Ridge, where the lithosphere is
modeled as a continuous as well as a fractured elastic
plate. These models are employed for a number of differ-
ent effective flexural rigidities where the corresponding
gravity effect of the models is used as a control to be
compared to the observed free-air anomalies. The results
show that for the continuous plate model a rigidity of
$(4.33 \pm 2.08) \times 10^{28}$ dyne-cm is required, whereas for
the fractured plate model a rigidity of $(2.0 \pm 1.0) \times 10^{29}$
dyne-cm is required. These rigidities are quite low and
correspond to plate thicknesses of 7.86 km and 13.1 km
respectively. On the other hand, if the lithosphere is
considered a viscoelastic plate and modeled as a continuous
elastic plate, the required thickness is in the range
40-70 km, and when modeled as a fractured elastic plate,
it is in the range 20-35 km. Seismic evidence indicates

that the 40-70 km range is quite reasonable, suggesting that the lithosphere can be modeled as the continuous visco-elastic plate described using continuous elastic plate theory. Using these results, data from a study by Watts and Cochran are reinterpreted and indicate that the litho-sphere thickens with age along the Hawaiian-Emperor Sea-mount Chain.

TABLE OF CONTENTS

Figure

INTRODUCTION

The concept of plate tectonics is based on the idea that the outer portion of the Earth consists of a rigid outer layer (lithosphere) overlying a weak substratum (asthenosphere). The existence of this kind of structure was first discussed by Barrell (1914a, 1914b, 1915) and has since become widely accepted.

In studies concerning the response of the lithosphere to various applied loads, it has been found that the lithosphere can be modeled as a body of finite strength. Furthermore, studies on the variation of seismic wave velocities and attenuation have shown that for loading times greater than 10^6 years, the asthenosphere can be modeled as a dense fluid (Walcott, 1976). In studying this problem, early researchers such as Gunn (1943a, 1943b, 1947, 1949), Vening-Meinesz (1941), Heiskanen and Vening-Meinesz (1958) and Jeffreys (1959) all considered the lithosphere as an elastic plate overlying a weak fluid. It was through these studies, which used either elastic beam or thin plate theory, that this method was found to work quite well. Later studies such as those by Walcott (1970a, 1970b, 1970c, 1972, 1976) investigated the response of the lithosphere due to applied loads which had existed for long periods of time. In his studies, he concludes that as the load gets older, the lithosphere responds viscoelastically rather than elastically and has a time constant on the or-

der of 10^5 years. In this manner, the rigidity of the
lithosphere will seem to decrease rather than remaining
constant as time increases.

More recently, studies have been made by Cochran
(1973), Watts and Talwani (1974), Watts and Cochran
(1974) and Watts, Cochran and Selzer (1975) who examined
the characteristic features of lithospheric response to
applied loads. In these studies, both two- and three-
dimensional deflection models have been made, all of which
have produced quite good results. The study made by
Watts and Cochran (1974) showed that for a large feature,
such as the Hawaiian-Emperor seamount chain, the effective
flexural rigidity, after some given time, seems to reach
a finite, nearly constant value when the lithosphere is
assumed to be of constant thickness. In all of these
studies, the parameter which is of greatest interest is
the effective flexural rigidity which represents a mea-
sure of the resistance of the lithosphere to deformation.

The feature of interest in this study is the Necker
Ridge which lies perpendicular to the Hawaiian Chain at
approximately 22°N latitude and 167°W longitude. The
purpose of this study is to (1) construct a bathymetric
as well as a gravity contour map utilizing the abundance
of new data available, and (2) to learn how the litho-
sphere responds to a small two-dimensional load both
elastically and viscoelastically.

DATA REDUCTION

Gravity and Bathymetry

The gravity and bathymetry data used for this study were obtained from surface-ship measurements made on the University of Hawaii vessel Kana Keoki between 1971 and 1975 as well as one cruise of the OSS Pioneer (U.S. Dept. of Commerce, 1964). A summary of particular cruise legs with their corresponding navigation and instrumentation, is given in Table 1.

From Table 1 we can see that all of the Kana Keoki cruises used the same gravimeter system, that being a LaCoste and Romberg air-sea gravimeter (S-33) mounted on a LaCoste and Romberg gyro-stabilized platform. For all of these cruises, satellite navigation was used and very accurate position fixes were obtained. Furthermore, to obtain a high accuracy, cross-coupling corrections were made yielding an accuracy for all of the data in the range of 2-4 mgal.

The data used from the OSS Pioneer were obtained with a LaCoste and Romberg air-sea gravimeter (S-11) mounted on a gimbal suspension. The observers estimated the accuracy as 12-15 mgal (U.S. Dept. of Commerce, 1964), where the navigation used was based on celestial fixes instead of satellite navigation. Because of this, as well as for reasons related to possible gimbal suspension meter errors

TABLE 1

CRUISE IDENTIFICATION, NAVIGATION AND INSTRUMENTATION

SHIP	YEAR	CRUISE AND LEG IDENTIFICATION	PROFILE NUMBER	NAVIGATION	GRAVIMETER	SUSPENSION
KANA KEOKI	1975	75072600	1	SATELLITE	L&R S-33	L&R GYROSTA-BILIZED PLATFORM
OSS PIONEER	1964	IIOE*-OPR442	2	CELESTIAL	L&R S-11	GIMBAL SUS-PENSION
KANA KEOKI	1972	72070201	3	SATELLITE	L&R S-33	L&R GYROSTA-BILIZED PLATFORM
KANA KEOKI	1971	71042601	4	SATELLITE	L&R S-33	L&R GYROSTA-BILIZED PLATFORM
KANA KEOKI	1973	73102500	5	SATELLITE	L&R S-33	L&R GYROSTA-BILIZED PLATFORM

*IIOE = INTERNATIONAL INDIAN OCEAN EXPEDITION

regarding sea state, it is felt that the above estimated accuracy is a valid one.

In reduction of the data to usable form, the bathymetry was converted to corrected meters using the velocity of sound in water as given in Matthews tables (1939). The gravity data used were in the form of free-air anomalies (FAA). These had been calculated relative to the Potsdam system, using the International Gravity Formula adopted in 1924 by the International Union of Geodesy and Geophysics.

The above data are presented in two forms: the first being bottom contour charts and the second being selected profiles. The control for the contour charts is shown in Figure 2 where it can be seen that there is a sparsity of bathymetric control in the southwest portion of the area and an overall sparsity of gravity control throughout the southern half of the area. The contour intervals for the charts were chosen as 100 m for the bathymetry to show the regional detail (Figure 3), and 25 mgal for the gravity (Figure 4). Control for the southwest portion of the bathymetry was taken from charts published by Chase, et al. (1970).

The particular profiles chosen were those relatively perpendicular to the Necker Ridge. These were then projected perpendicular to the ridge as shown in Figure 1 and plotted as shown in Figure 5. From Figure 1 it can be seen that profiles 1, 2, 4 and 5 are all at approximately the same areal direction orientation and are relatively

6

Figure 1. Location of selected profiles used for this
           study across the Necker Ridge. Bathymetry is
           at 200 fm intervals, from Chase et al. (1970).

8
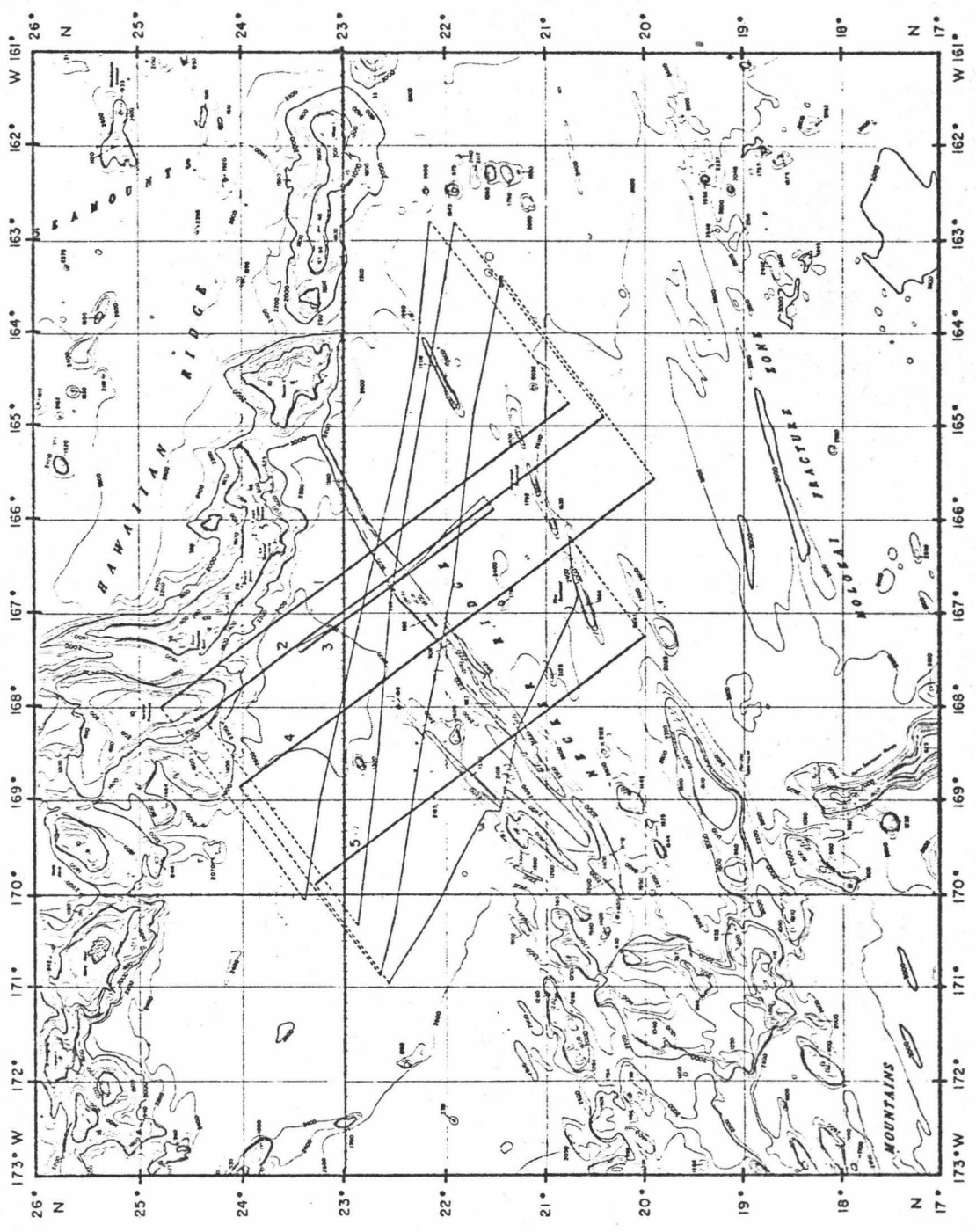
Figure 2.   Ship tracks used to construct the bathymetry
            and gravity contour maps (Figures 3 and
            4) for the Necker Ridge area.   The solid
            lines represent gravity control while all
            of the lines represent bathymetry control.
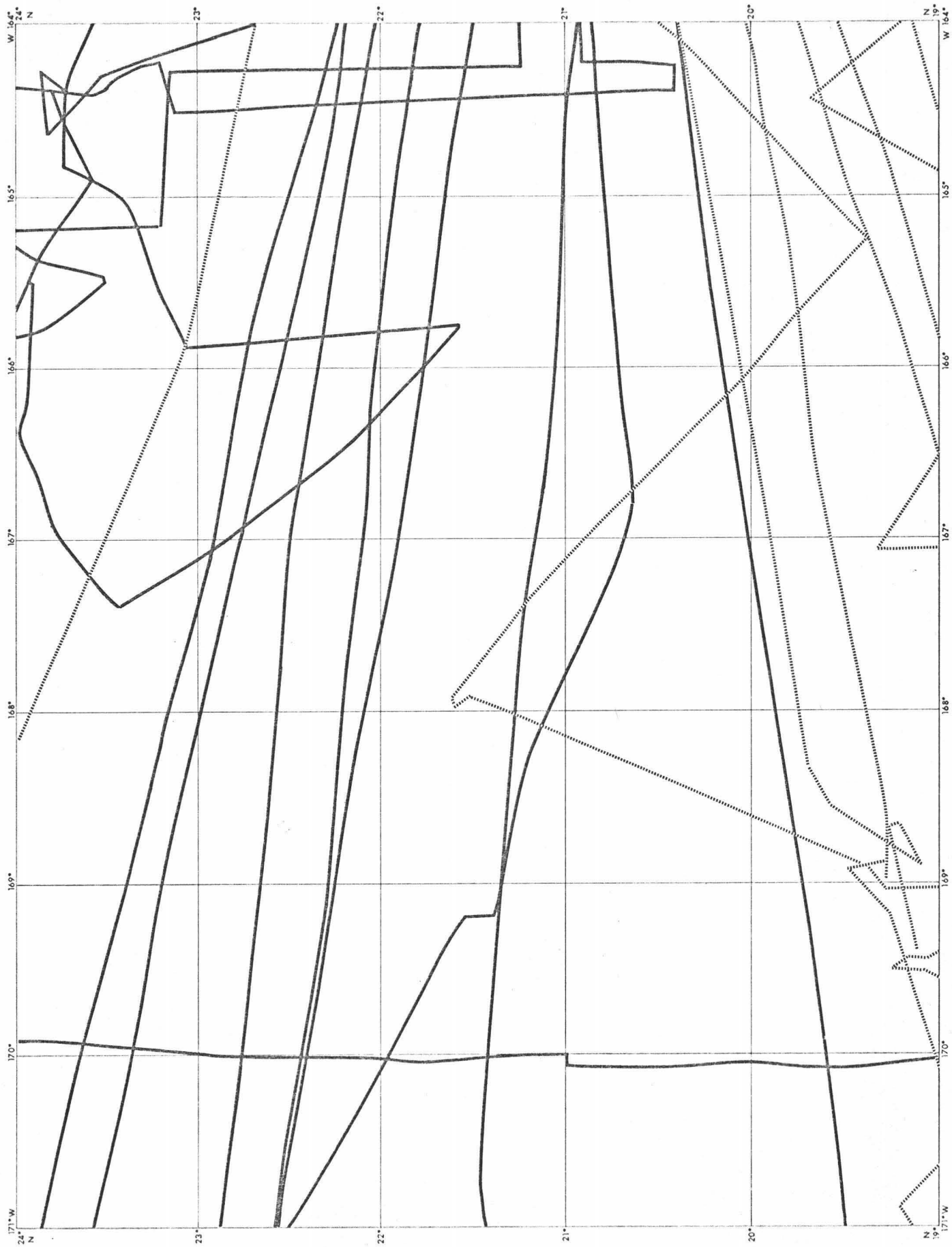
Figure 3. Bathymetry of the Necker Ridge with a contour
interval of 100 m in the flatter areas. Con-
trol for the southwest portion of the map
was based on Chase et al. (1970).

12
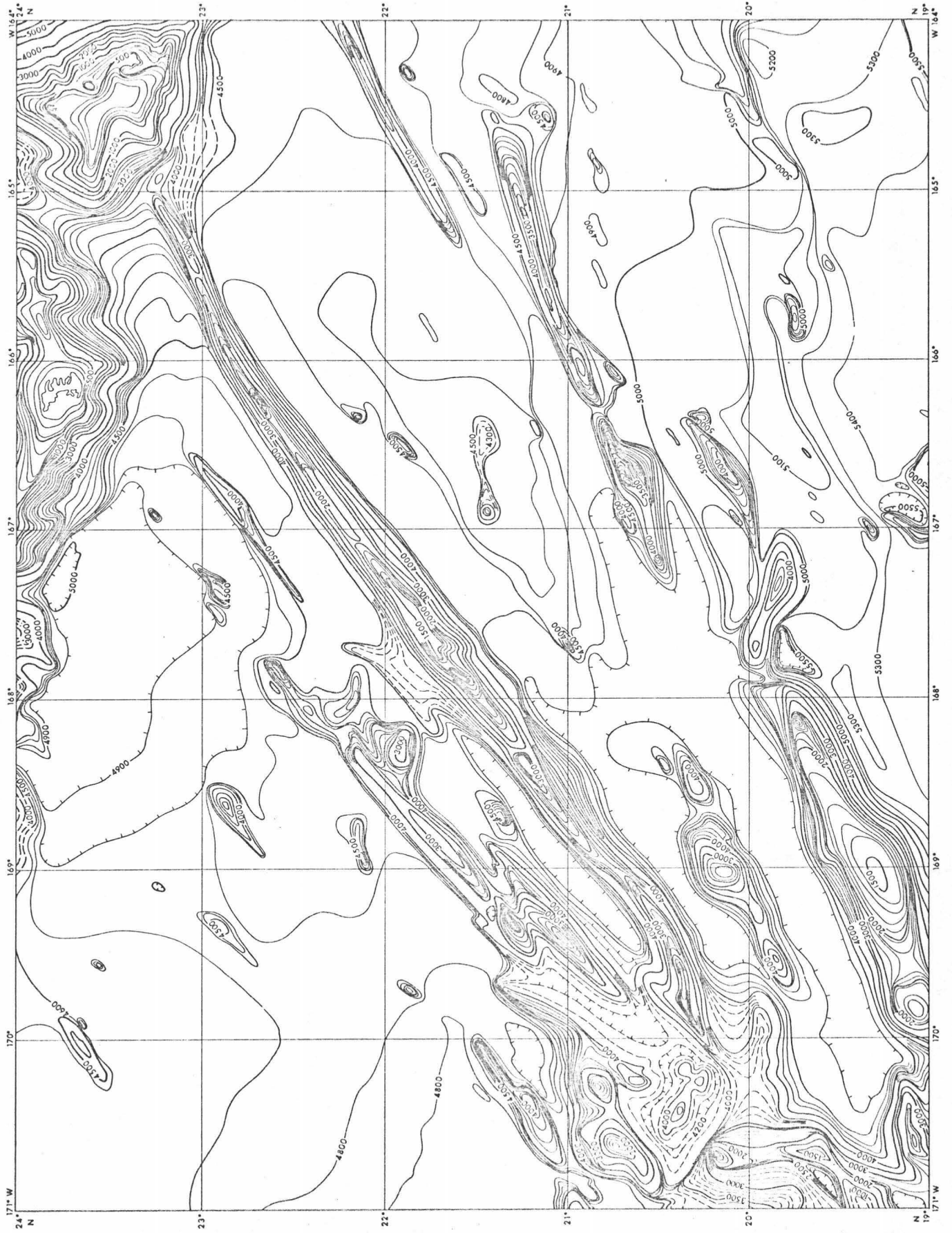
Figure 4. Free-air anomaly map of the Necker Ridge area
with a contour interval of 25 mgal.

Figure 5. Observed topography and observed free-air
anomaly for the profiles chosen (see Figure
1). All the profiles shown represent pro-
jected profiles running perpendicular to the
trend of the Necker Ridge where the gravity
profiles were reduced using the International
Gravity Formula adopted in 1924.

OBSERVED TOPOGRAPHY

OBSERVED FAA
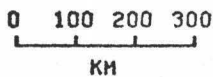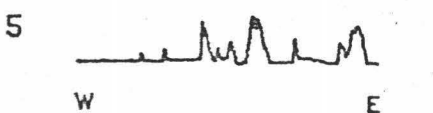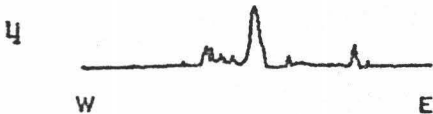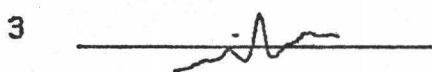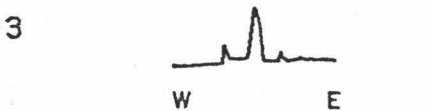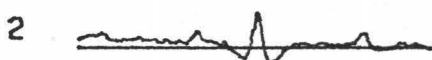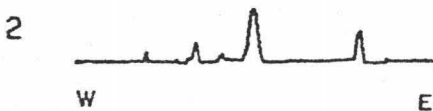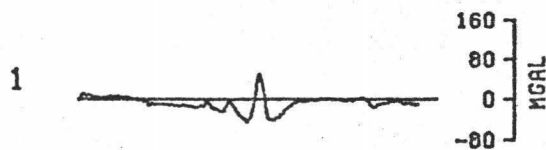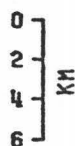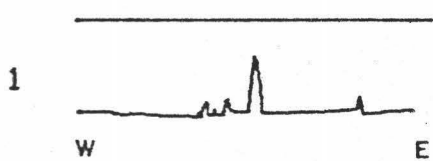
parallel to the Hawaiian Chain, while profile 3 is at a totally different azimuth running more nearly perpendicular to the Hawaiian Chain. For this reason, the west end of gravity profile 3 is more negative than the rest since in approaching the Hawaiian Chain it enters the negative FAA belt which flanks the entire Hawaiian Chain (Watts and Cochran, 1974). Other than this, all of the gravity profiles are quite similar with a negative FAA belt flanking either side of the ridge and an average anomaly amplitude on the order of 40 mgal. The positive anomalies all correspond closely with topography, and reach a maximum value of about 100 mgal.

Sediment Thickness and Density Determination

In determining the thickness of the sediment in a given area, the reflection seismic record is needed in order to obtain the one way travel time, and an interval velocity for the sediment is required. For this study, of the five profiles considered, seismic reflection records were available for only three of them, i. e., profiles 1, 3 and 5, and, due to a lack of dependable near-surface refraction data, the sediment interval velocity was unknown.

To determine the interval velocity, there are three primary methods used (Hamilton, et al., 1974): (1) assume an interval velocity for the sediment, (2) use an equation

or curve calculated for a similar area, or (3) use a pre-
dicted initial velocity for the surface of the sediments,
V_0, and a corresponding velocity gradient.

Since sediment velocity generally increases with
depth of burial, it is obvious that the average velocity
of the sediment will increase with sediment thickness.
For this reason, an overall interval velocity should not
be used over all areas, but rather should be averaged in-
dependently for different sediment wedges dependent on
their relative thickness.

In this study, method (3) above was used to calculate
the thickness and interval velocity of each reflection
point picked. These interval velocities were then averaged
over each sediment wedge to obtain an average interval
velocity from which the average density could be obtained
for the sediment wedges.

Houtz and Ewing (1963) determined an empirical formula
for the variation of sound velocity in sediments given by

$$V = V_0 + ah ,$$

where V_0 represents the velocity at the liquid sediment
interface, a is the average velocity gradient dependent
on time, and h is the thickness of the layer. Solving
this for h gives

$$h = V_0 (\exp(at) - 1)/a$$
$$= V_0 t + (aV_0)t^2/2 + (a^2V_0)t^3/6 + . . . ,$$

where for small one-way reflection time t, this can be approximated by

$$h = V_0 t + (aV_0) t^2/2 \; ,$$

and from this, we get for the velocity at a depth h

$$V = V_0 + (aV_0) t \; .$$

The average value for V_0 used here was 1.52 km/sec (Hamilton, 1970, 1971, 1973; Hamilton, et al., 1974; Houtz, et al., 1968, 1970), and for a, we used the relation given by Hamilton, et al. (1974) which represents a polynomial regression of data obtained over 13 areas covering a region extending from the Northern Pacific to the Indian Ocean. The relation is given by

$$a = 1.318 - 1.4632t + 0.7135t^2 \; .$$

Next, to obtain an empirical way to determine the density, the density-velocity curve presented by Ludwig, et al. (1968) was digitized and a polynomial regression was run on it yielding the relation given in Table 2, accurate to 0.01 gm/cc. This relation is plotted in Figure 6, from which the sediment density was determined using the above calculated average interval velocity. The average velocity, density and thickness vs. one-way reflection time are plotted in Figures 7, 8 and 9 respectively.

Table 2

Empirical density-velocity
relationship with ρ in gm/cc and
V in km/sec

$$\rho = \sum_{n=0}^{8} a_n \, V^n$$

n	a_n
0	-2.724942402967010
1	6.479501873911820
2	-3.861248058096400
3	1.320642304407480
4	-0.274000161856168
5	0.034996857680028
6	-0.002672295209909
7	0.000111574589798
8	-0.000001956917160

Figure 6. Empirical Ludwig et al. (1968) density-
velocity curve shown as an 8th degree
polynomial regression fit, accurate to 0.01
gm/cc.

8TH DEGREE FIT

22
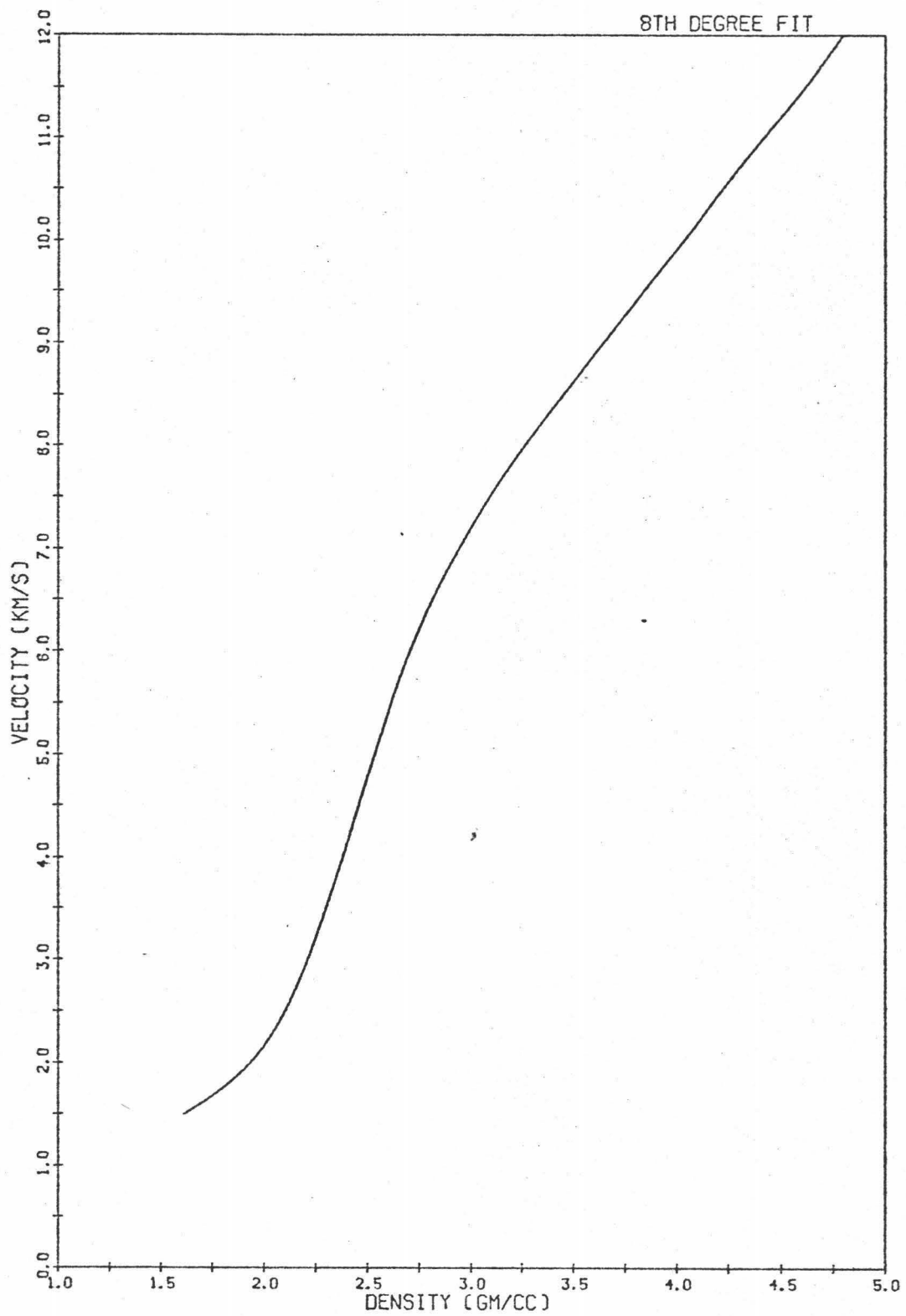
Figures 7 and 8. The average interval velocity and average density vs. one-way travel time assuming an initial velocity at the surface of 1.52 km/sec and a velocity gradient dependent on the travel time.

24
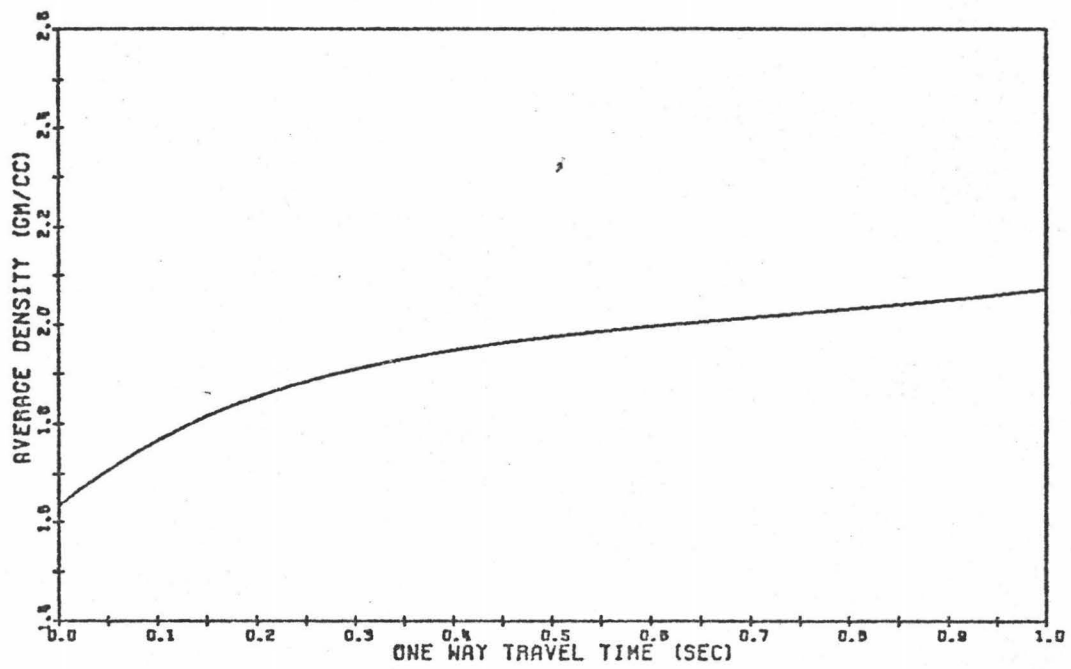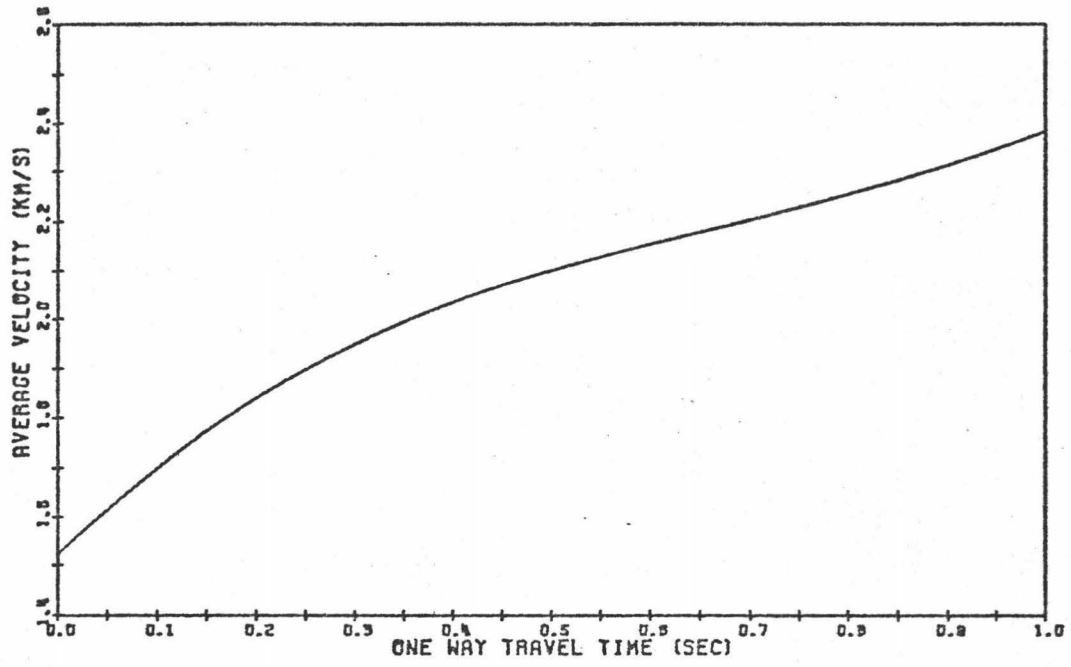
Figure 9. Sediment thickness vs. one-way travel time,
assuming an initial velocity at the surface
of 1.52 km/sec and a velocity gradient de-
pendent on the travel time.
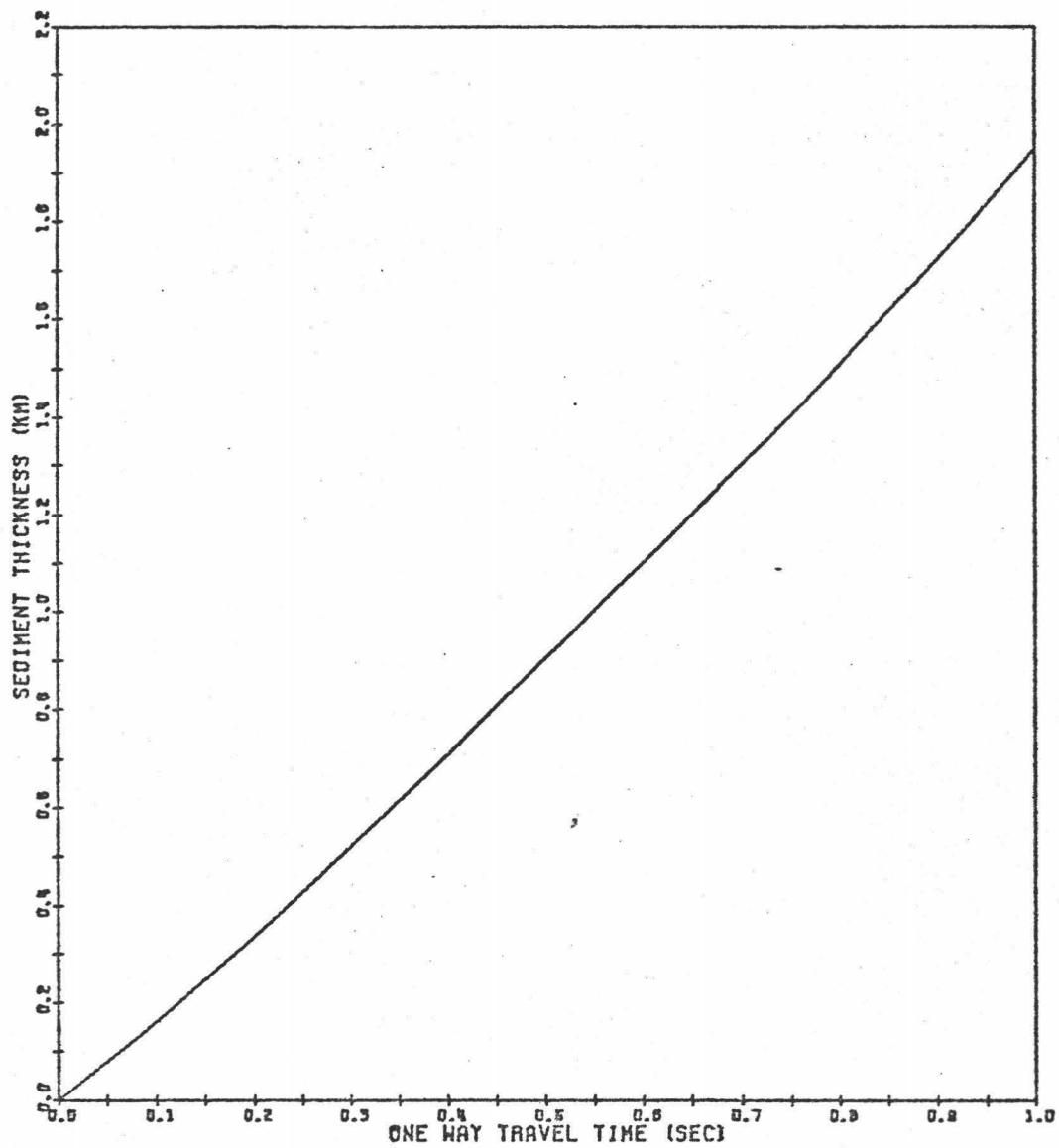
Using the calculated sediment thicknesses and average density, a Talwani two-dimensional program was used (Talwani, 1959) to remove the attraction of the sediment from the observed free-air anomaly. The corrected topography and free-air anomaly are plotted in Figure 10.

Finally, to determine the average density of the load material, a marine equivalent of the Nettleton (1939) "density profile" was determined for the profiles across the ridge. For the marine situation, this involved correcting the free-air gravity anomaly profiles on a two-dimensional basis for the gravity effect of the ridge, assuming a series of different densities contrasted with that of water. The corrected anomaly which showed the least correlation with the topography was then adopted as the one characterizing the true density and is termed here as the "Complete Free-Air Anomaly". This anomaly, for the marine case, represents the direct equivalent of the "Complete Bouguer Anomaly" implied in the Nettleton "density profile" method of determining the density of a non-marine topographic feature.

Since sediment calculations could not be made on all of the profiles, a marine density profile was run on the data both before and after removal of the sediment effect in order to see how the sediment layer would affect it. These results are shown in Figures 11 and 12. From Figure 11 (before the sediment correction) the average load density

seems to lie in the range 2.4-2.5 gm/cc, whereas from Figure 12 (after correcting for the sediment) the density seems to lie closer to 2.4 gm/cc. Thus, for this study, a load density of 2.4 gm/cc was used for the deflection models.

28

Figure 10. Basement topography, representing the observed

topography minus the sediment layer, with

its corresponding free-air anomaly corrected

for the gravitational attraction of the

sediment layer.
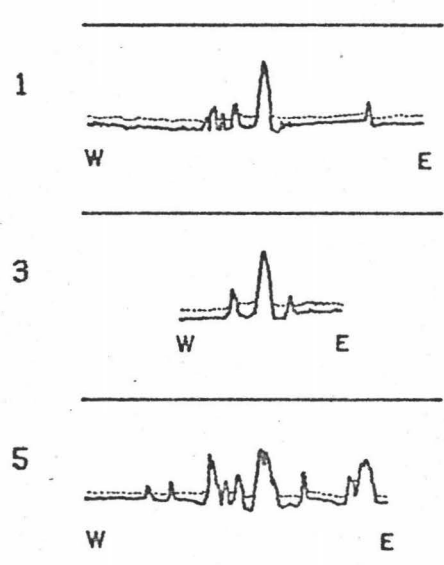
BASEMENT TOPOGRAPHY   CORRECTED FAA
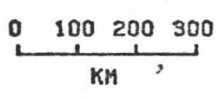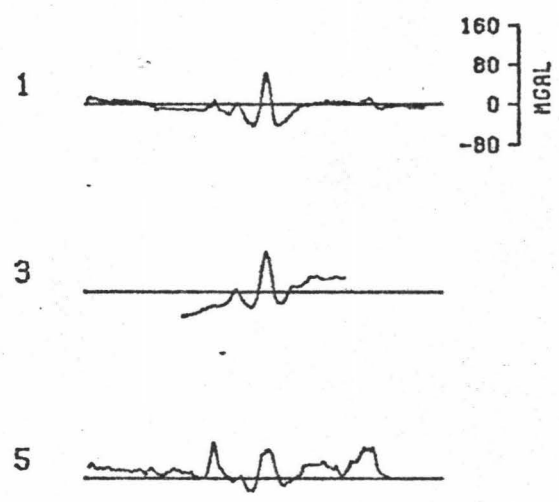
Figure 11. Marine density profiles of the observed free-
air anomalies utilizing the observed topo-
graphy for profiles 1, 2, 3, 4 and 5. These
curves represent "Complete Free-Air Anomalies".

DENSITY PROFILE

MGAL

2.0

3.0

1

DISTANCE FROM RIDGE AXIS (KM)

DENSITY PROFILE

MGAL

2.0

3.0

2

DISTANCE FROM RIDGE AXIS (KM)

DENSITY PROFILE

MGAL

2.0

3.0

3

DISTANCE FROM RIDGE AXIS (KM)

32
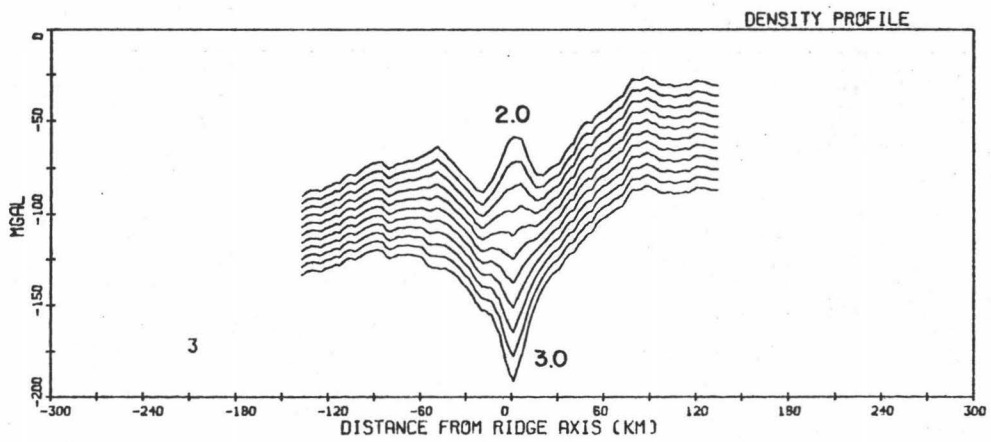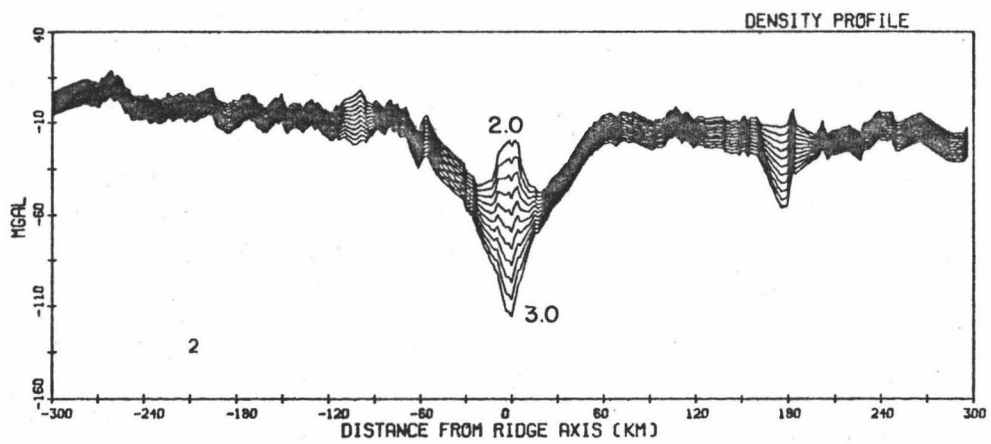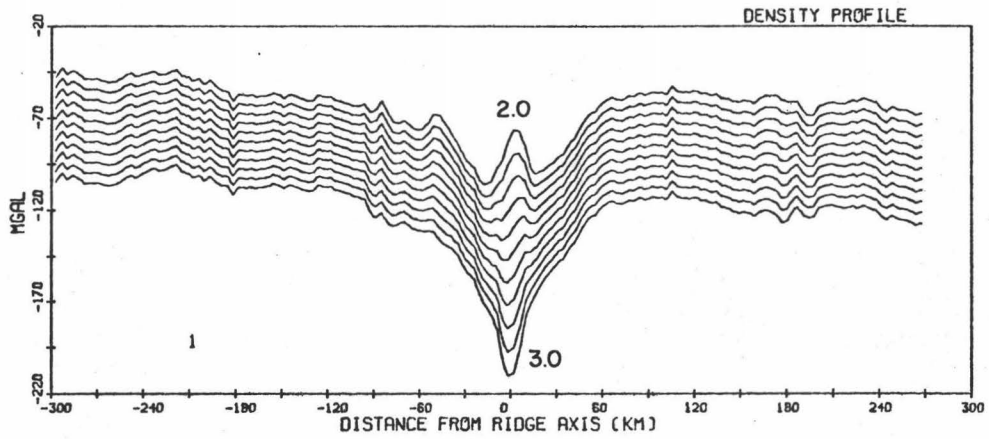
Figure 11. (Continued) Marine density profiles of the
observed free-air anomalies utilizing the
observed topography for profiles 1, 2, 3,
4 and 5. These curves represent "Complete
Free-Air Anomalies".

DENSITY PROFILE

2.0

3.0

4

MGAL

DISTANCE FROM RIDGE AXIS (KM)

DENSITY PROFILE

2.0

3.0

5

MGAL

DISTANCE FROM RIDGE AXIS (KM)

34
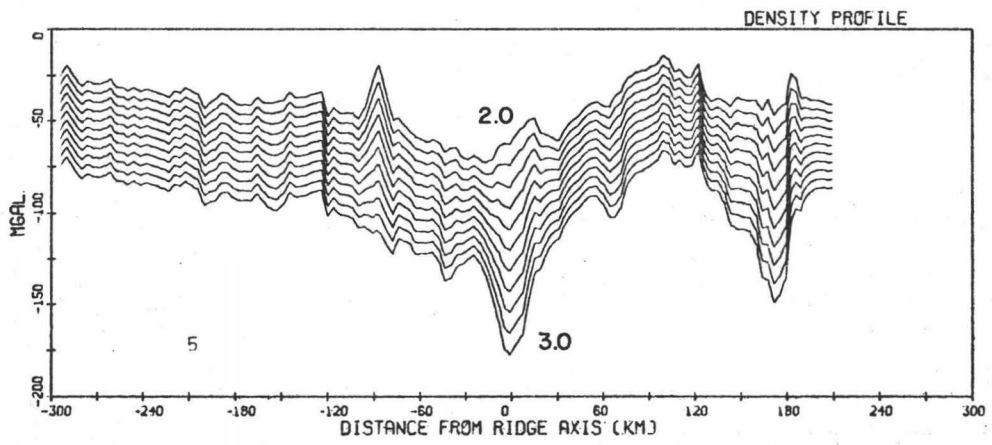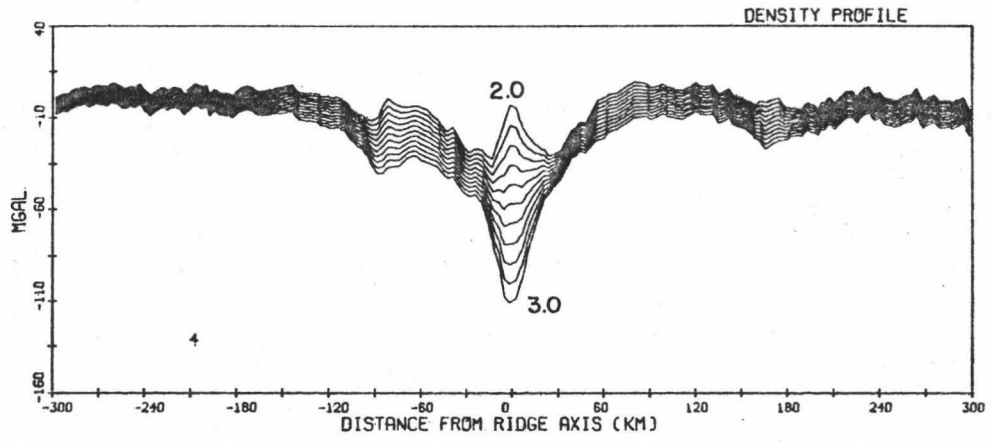
Figure 12. Marine density profiles of the corrected
free-air anomalies utilizing the basement
topography for profiles 1, 3 and 5. These
curves represent "Complete Free-Air Anomalies".

DENSITY PROFILE

(three stacked gravity/density profile plots, each labeled "DENSITY PROFILE", with y-axis "MGAL" and x-axis "DISTANCE FROM RIDGE AXIS (KM)"; curves labeled 2.0 and 3.0; panels numbered 1, 3, and 5)
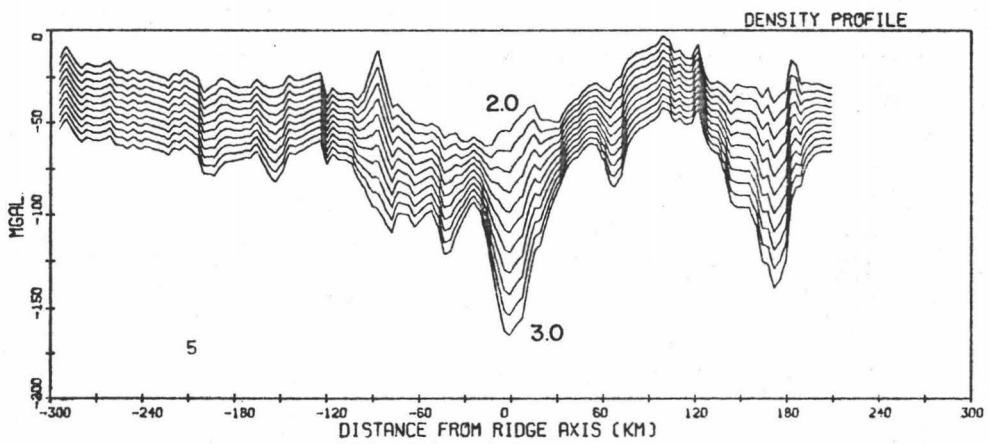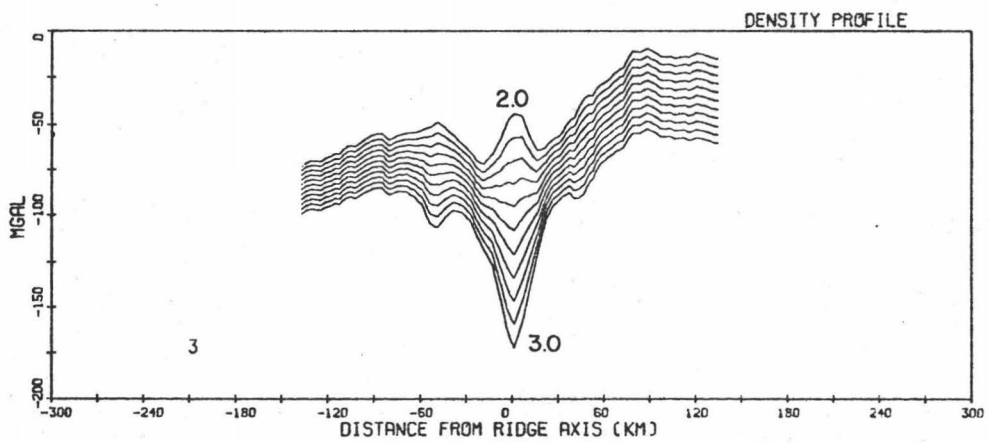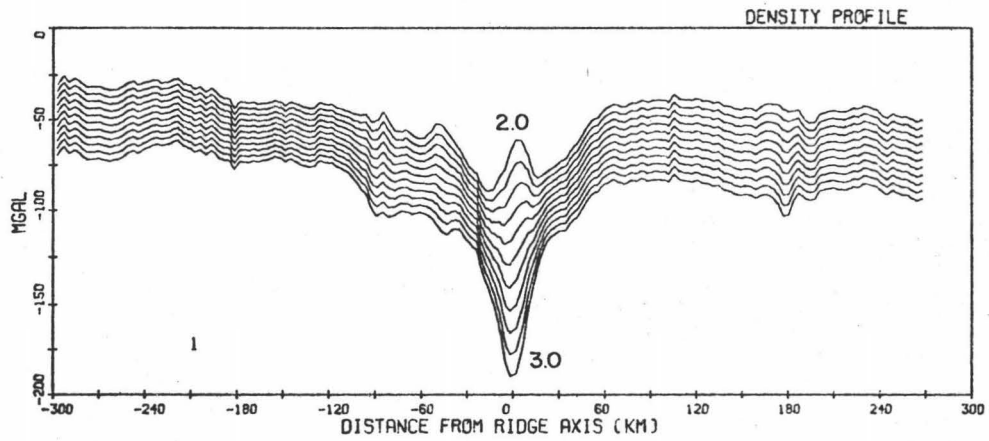
THEORY FOR THE DEFLECTION OF A LOADED LITHOSPHERE

Elastic Model

Here we will consider the lithosphere as an elastic plate overlying an asthenosphere of negligible strength subjected to a two-dimensional load. The differential equation governing the deflection is (see Appendix)

$$D \frac{d^4 w}{dx^4} + (\rho_3 - \rho_2)\, gw = P \tag{1}$$

where P   is an applied two-dimensional line load

      g   is the acceleration of gravity

      ρ_2 is the density of the material infilling the deflection

      ρ_3 is the density of the material underlying the sheet

      w   is the deflection

      x   is the horizontal distance from the point at which the load is applied

      D   is the effective flexural rigidity of the plate defined as

$$D = EH^3 / [12(1 - \sigma^2)] \tag{2}$$

where E   is Young's Modulus

      σ is Poisson's ratio

      H   is the effective thickness of the plate.

In order to solve this we will first find the homogeneous solution and then a particular solution depending on the model chosen. Thus, to obtain the homogeneous

solution, we let $P = 0$ and solve the above Equation 1 to give

$$w = e^{\lambda x}(Z_1 \cos\lambda x + Z_2 \sin\lambda x) + e^{-\lambda x}(Z_3 \cos\lambda x + Z_4 \sin\lambda x),$$

where $\quad\quad \lambda = [(\rho_3 - \rho_2)g/4D]^{1/4}$ \hspace{2cm} (3)

and Z_1, Z_2, Z_3 and Z_4 are constants of integration.

Considering the plate to be very large, it is a reasonable assumption that at a large distance from the application of the load, the deflection approaches zero. Thus, we can let $Z_1 = Z_2 = 0$.

We can then find a relationship between the remaining constants by considering the symmetry about the point at which the load is applied. That is, that the slope of the deflection will be zero at $x = 0$ giving $Z_3 = Z_4 = C$, yielding finally

$$w = C\, e^{-\lambda x}(\cos\lambda x + \sin\lambda x)\,. \hspace{1cm} (4)$$

Next, consider the particular case of an applied line load P on the plate (Hetenyi, 1946). In order to have stability, the load P will have to be in equilibrium with the buoyancy forces $(\rho_3 - \rho_2)gw$, which leads to the conditional equation

$$\int_{-\infty}^{\infty} (\rho_3 - \rho_2)gw\, dx = P, \hspace{1cm} (5)$$

or upon substitution of (4) into (5) gives

$$C = P\lambda/[2(\rho_3 - \rho_2)g]$$

or upon substitution of (4) into (5) gives

$$C = P\lambda / [2(\rho_3 - \rho_2)g]$$

leading to the deflection equation

$$w = \frac{P\lambda}{2(\rho_3 - \rho_2)g} e^{-\lambda x}(\cos\lambda x + \sin\lambda x) \tag{6}$$

Since most of the loads observed in nature are those of distributed loads, it therefore is important to look at the deflection of the lithosphere due to a distributed load in contrast to a line load. To do this, we consider the load as consisting of a series of thin, infinitely narrow sections, each producing a concentrated downward force of $P = p\,dx$. The deflection dw for one such section can then be modeled using our previously defined relation for a concentrated line load yielding:

$$dw = \frac{p\lambda}{2(\rho_3 - \rho_2)g} e^{-\lambda x}(\cos\lambda x + \sin\lambda x)\,dx$$

from which we obtain the total deflection of our load both under and to the side of the load by integrating over the respective limits.

For a point under the load we get

$$w_1 = \frac{p}{2(\rho_3 - \rho_2)g}[2 - e^{-\lambda R}\cos\lambda R - e^{-\lambda r}\cos\lambda r], \tag{7}$$

for a point to the left of the load we get

$$w_2 = \frac{p}{2(\rho_3 - \rho_2)g}[e^{-\lambda R}\cos\lambda R - e^{-\lambda r}\cos\lambda r], \tag{8}$$

and for a point to the right of the load we get, by
symmetry

$$w_3 = -w_2 \quad , \tag{9}$$

where here R is the distance from the left end of the load
to the point and r is the distance from the right end of
the load to the point.

A comparison of the deflection produced by a given
load, modeled first as a line load and then as a distributed
load is given in Figure 13. Here it is seen that the line
load approximation produces both larger amplitude as well
as a shorter wavelength deflection in comparison to the
distributed load. Thus to calculate the deformation more
accurately, this study will consider the distributed load
case, hereafter referred to as Model I. It should be
noted here that for a small load such as the Necker Ridge,
the two models actually produce quite similar results al-
though for maximum accuracy, the distributed model is
still used.

A second model also considered in this study is that
of a vertically fractured lithosphere (Model II). To
summarize the method by which the deflection equation is
derived it is convenient to consider first an infinite
plate subjected to a line load at the origin. This load
will produce, at the origin, a bending moment, M, and
a shearing force, Q. Thus the removal of both M and Q
would be the same as removing half the plate, creating a

Figure 13. Continuous elastic plate deflection due to
a given load modeled as a line load and as
a distributed load.

41

TOPOGRAPHY

DEFLECTION

0 50 100 150 200
KM
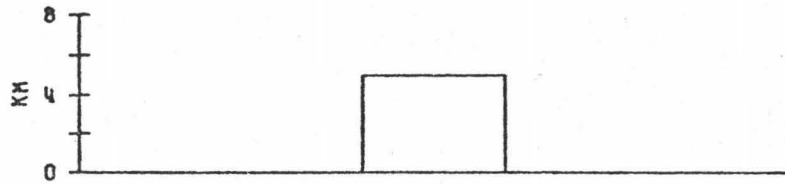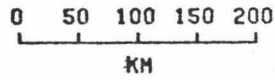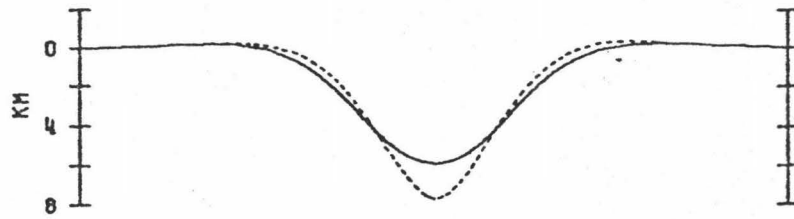
---------- LINE LOAD
———— DISTRIBUTED LOAD

free end at the origin. This is done by applying simul-
taneously a moment and force at the origin which produce
a bending moment, -M, and a shearing force, -Q, (Hetenyi,
1946). Then by placing two of these semi-infinite plates
together we obtain a model for an infinite plate fractured
at the origin. We can further, by the principle of super-
position, add a distributed load to the plate from which
we obtain our deflection equation.

In this study I have chosen the origin to coincide
with the fracture, with the distance, x, measuring positive
to the right, representing the distance from the origin
to the point at which the deflection is to be calculated.
Thus for a load of width ℓ, a distance s from the origin
(always positive), the deflection is broken up into three
cases:

1) for a point to the left of the load

$$w = \frac{p}{2(\rho_3 - \rho_2)g} \{[e^{-\lambda s}(\cos\lambda s - 2\sin\lambda s) +$$

$$e^{-\lambda(s+\ell)}(2\sin\lambda(s+\ell) - \cos\lambda(s+\ell))] \; .$$

$$e^{-\lambda x}(\cos\lambda x + \sin\lambda x) + [e^{-\lambda s}(3\sin\lambda s -$$

$$\cos\lambda s) - e^{-\lambda(s+\ell)}(3\sin\lambda(s+\ell) - \cos\lambda(s+\ell))] \; . \quad (10)$$

$$e^{-\lambda x}\sin\lambda x + [e^{-\lambda(s-x)}\cos\lambda(s-x) - e^{-\lambda(s+\ell-x)} \; .$$

$$\cos\lambda(s+\ell-x)]\}$$

2) for a point under the load

$$w = \frac{p}{2(\rho_3 - \rho_2)g} \{[e^{-\lambda s}(\cos\lambda s - 2\sin\lambda s) +$$

$$e^{-\lambda(s+\ell)}(2\sin\lambda(s+\ell))] \; .$$

$$e^{-\lambda x}(\cos\lambda x + \sin\lambda x) + [e^{-\lambda s}(3\sin\lambda s -$$

$$\cos\lambda s) - e^{-\lambda(s+\ell)}(3\sin\lambda(s+\ell) - \cos\lambda(s+\ell))] \cdot \qquad (11)$$

$$e^{-\lambda x}\sin\lambda x + [(1 - e^{-\lambda(x-s)}\cos\lambda(x-s)) +$$

$$(1 - e^{-\lambda(s+\ell-x)}\cos\lambda(s+\ell-x))] \}$$

3) for a point to the right of the load

$$w = \frac{p}{2(\rho_3-\rho_2)g} \{[e^{-\lambda s}(\cos\lambda s - 2\sin\lambda s) +$$

$$e^{-\lambda s+\ell)}(2\sin\lambda(s+\ell) - \cos\lambda(s+\ell))] \cdot$$

$$e^{-\lambda x}(\cos\lambda x + \sin\lambda x) + [e^{-\lambda s}(3\sin\lambda s - \qquad (12)$$

$$\cos\lambda s) - e^{-\lambda(s+\ell)}(3\sin\lambda(s+\ell) - \cos\lambda(s+\ell))] \cdot$$

$$e^{-\lambda x}\sin\lambda x - [e^{-\lambda(x-s)}\cos\lambda(x-s) - e^{-\lambda(x-s-\ell)} \cdot$$

$$\cos\lambda(x-s-\ell)] \}$$

These deflection equations are now in a convenient
form which can be applied easily to any irregularly shaped
load. This is done by dividing the load up into a series
of two-dimensional columns whose height, h, is measured from
mean sea floor. The individual loads, p, are then calculated
using the relation

$$p = h (\rho_1 - \rho_0) g , \qquad (13)$$

where here ρ_1 is the density of the load material and ρ_0
is the density of the surrounding medium. Then to determine
the total deflection, we sum all of the deflection curves
due to each column using the principal of superposition
(Hetenyi, 1946).

In Figure 14 the deflection curves for the assumed
load shown are plotted for the parameters listed below in
Table 3.

Table 3

Assumed parameters for
Models I and II (Figure 14)

ρ_0 = 1.03 gm/cc

ρ_1 = 2.40 gm/cc

ρ_2 = 2.40 gm/cc

ρ_3 = 3.40 gm/cc

g = 980 cm sec^{-2}

D = 2 10^{29} dyne-cm

λ = 1.87 10^{-7} / cm

The load here represents a two-dimensional ridge
broken up into 16 sections, each 2 km wide, reaching a
maximum height of 3 km. The density of the load was
assumed to be 2.4 gm/cc as discussed earlier, while the
density of the material infilling the deflection is assumed
to be the same as the load. For the substratum the assumed
density of 3.4 gm/cc represents an average density similar
to that used by Vening-Meinesz (1941), Walcott (1970c),
and Watts and Cochran (1974).

Another parameter which can be looked at is the effec-
tive thickness of the plate H, which can be found from
the definition of the flexural rigidity giving

$$H = [12 D (1 - \sigma^2) / E]^{1/3} , \qquad (14)$$

45

Figure 14. Deflection curves for two simple models;
Model I being a continuous elastic litho-
sphere and Model II being a fractured elastic
lithosphere. The load represents a two-
dimensional distributed load as shown, with
the model parameters given in Table 3.

TOPOGRAPHY

MODEL I

MODEL II

0 50 100 150 200
KM
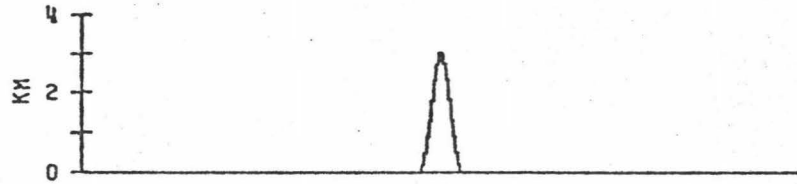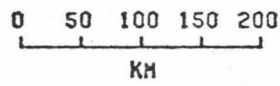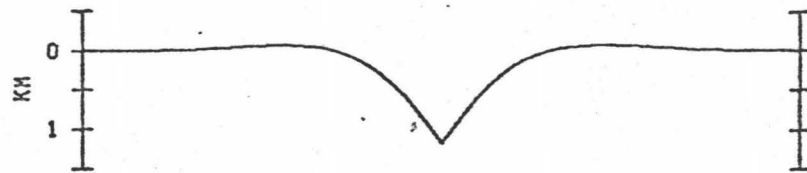
where for the above model·

$$D = 2 \ 10^{29} \ \text{dyne-cm}$$

$$E = 10^{12} \ \text{dyne cm}^{-2}$$

$$\sigma = 0.25$$

we have $\quad\quad\quad H = 13.1 \ \text{km}$.

It should be noted here that this thickness represents only an effective thickness and may not correspond to the true thickness of the plate.

Viscoelastic Model

Here we consider the lithosphere as a viscoelastic body instead of an elastic one which, as before, overlies a weak asthenosphere (Walcott, 1970a; Watts and Cochran, 1974). An important aspect of a viscoelastic body is that when subjected to a constant load, it initially responds as an elastic body followed by a slow viscous flow. Thus if we were to describe this physical model using the previously derived equation for an elastic lithosphere, then as the age of loading increases, the effective flexural rigidity needed to match the true deformation would have to decrease.

The equation governing the deflection in this case, for a viscoelastic plate overlying a weak fluid is (Nadai, 1963)

$$D_0 \ \frac{d^4 \overset{o}{w}}{dx^4} + (\ \rho_3 - \rho_2) g [\ \overset{o}{w} + \frac{w}{\tau}\ ] = \overset{o}{P} + \frac{P}{\tau} \ , \quad\quad (15)$$

where w, x, ρ_2, ρ_3, g and P are defined the same as for

Equation 1. D_0 represents the instantaneous effective flexural rigidity (Watts and Cochran, 1974). The dot represents the first derivative with respect to time and τ represents the relaxation time defined as

$$\tau = 3\eta(1 - \sigma^2) / E ,$$

where η is the effective viscosity of the plate.

As before, in order to solve this we first consider just the homogeneous equation which is obtained by letting $P = \overset{\circ}{P} = 0$. Then our solution is of the form

(16)
$$w = e^{t/\tau_0} [e^{\gamma x}(Z_1\cos\gamma x + Z_2\sin\gamma x) + e^{-\gamma x}(Z_3\cos\gamma x + Z_4\sin\gamma x)],$$

where Z_1, Z_2, Z_3 and Z_4 are constants of integration, γ is a constant derived from the separation of variables and

$$\tau_0 = \tau[(\frac{\gamma}{\lambda})^4 - 1] ,$$

where λ is the same as in Equation 3.

If we then assume the same boundary conditions as before we have

1) as $x \to \infty$, $w \to 0$ $\quad \Rightarrow \quad$ $Z_1 = Z_2 = 0$,

2) $[\frac{dw}{dx}]_{x=0} = 0$ $\quad \Rightarrow \quad$ $Z_3 = Z_4 = V_0$.

Thus our deflection equation now becomes

$$w = V e^{-\gamma x}(\cos\gamma x + \sin\gamma x) , \qquad (17)$$

where $V = V_0\exp(t/\tau_0)$ represents the maximum deflection of the plate at $x = 0$. This has been solved by Nadai (1963) for an applied line load P. The solution obtained

assumes that the plate is initially subjected to the load P very rapidly such that its initial response is purely elastic producing a deflection w_0 governed by Equation 6 :

$$w_0 = \frac{P\lambda}{2(\rho_3-\rho_2)g} \quad e^{-\lambda x}(\cos\lambda x + \sin\lambda x) \; ,$$

followed after a time, t, given by

$$t = \frac{\tau}{4} \left[\left(\frac{\gamma}{\lambda}\right)^4 - 1 - \ln\left(\frac{\gamma}{\lambda}\right)^4 \right] \; , \tag{18}$$

by the deflection

$$W = \frac{P}{2(\rho_3-\rho_2)g} \quad \left[\frac{1}{x} \left(e^{-\lambda x}\cos\lambda x - e^{-\gamma x}\cos\gamma x\right) \right.$$

$$\left. -\lambda e^{-\lambda x}(\cos\lambda x + \sin\lambda x) \ln\left(\frac{\gamma}{\lambda}\right) \right] \qquad (x\neq 0) \tag{19}$$

$$V = \frac{P\lambda}{2(\rho_3-\rho_2)g} \quad \left[\left(\frac{\gamma}{\lambda}\right) - 1 - \ln\left(\frac{\gamma}{\lambda}\right) \right] \qquad (x=0)$$

where, in general, we define the total deflection as

$$w = \begin{cases} w_0 + W & (x \neq 0) \\ [w_0]_{x=0} + V & (x = 0) \end{cases} \tag{20}$$

To compute the above line load it is convenient to use the equation

$$P = g(\rho_1-\rho_0) \left((B - A) C + 2AC \right) \tag{21}$$

where A represents the half width of the load at its top,

B represents the half width of the load at its base and C represents the height of the load.

To see how Equation 20 varies with time, it has been plotted in Figure 15 for various values of t/τ and the parameters listed in Table 4. These curves are plotted such that their amplitudes are normalized to the initial elastic deflection.

Table 4

Assumed parameters for
Viscoelastic Model (Figure 15)

$$\rho_0 = 1.03 \text{ gm/cc}$$

$$\rho_1 = 2.40 \text{ gm/cc}$$

$$\rho_2 = 2.40 \text{ gm/cc}$$

$$\rho_3 = 3.40 \text{ gm/cc}$$

$$g = 980 \text{ cm sec}^{-2}$$

$$D_0 = 3.8 \ 10^{31} \text{ dyne-cm}$$

$$A = 2 \text{ km}$$

$$B = 16 \text{ km}$$

$$C = 3 \text{ km}$$

From this plot it can be seen that as t/τ increases, the amplitude also increases while the wavelength decreases. Or, in effect, as the age of loading increases, both the wavelength and amplitude of the anomalous free-air anomaly will tend to decrease.

Gravity Effect of Models

In calculating the gravity effect of the deflection

51

Figure 15. Deflection throughout time, of a continuous
viscoelastic plate under a constant line load
representing the average load of the Necker
Ridge. The deflection curves are all normalized
to the initial elastic deflection, given
by curve 1, where the assumed model parameters
are given in Table 4.
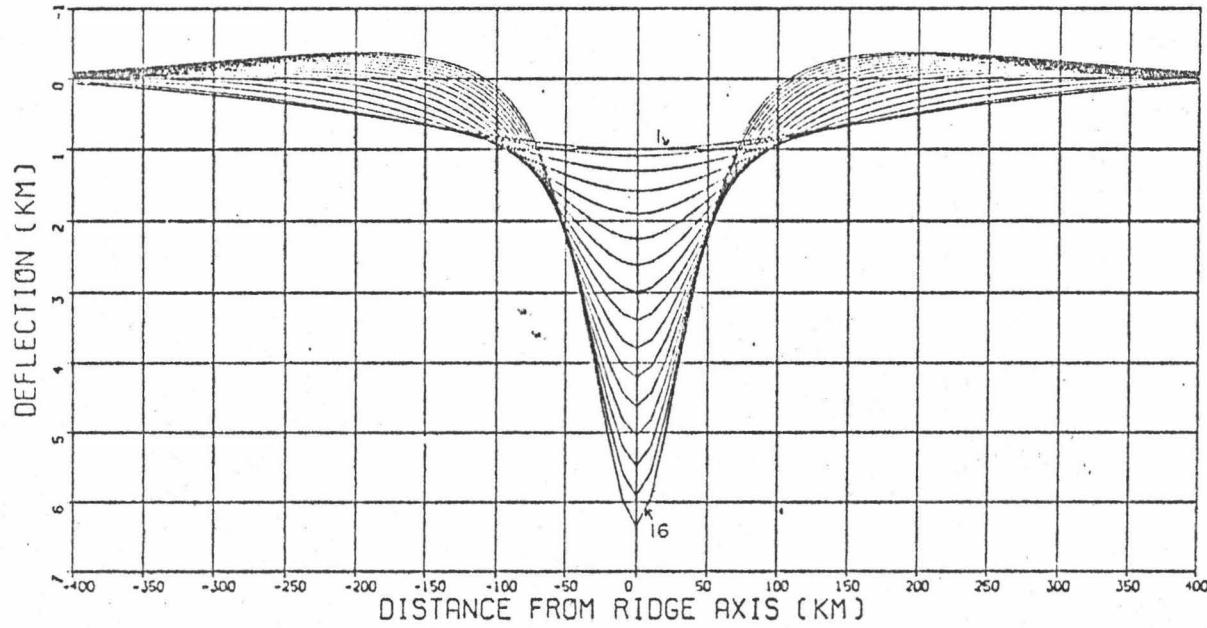
CURVE	t/τ
1	0.00
2	0.61
3	3.06
4	8.59
5	18.90
6	36.01
7	62.36
8	100.76
9	154.39
10	226.81
11	321.96
12	444.14
13	598.05
14	788.75
15	1021.67
16	1302.63

models to compare them with those observed, we first found
the effect of the load alone and then added on to this the
effect due to the deflection. The gravity effect of the
load was calculated using a Talwani two-dimensional program
over the observed topography assuming a uniform density of
2.4 gm/cc for the load material and a density of 1.03 gm/cc
for the sea water.

To calculate the total effect of the deflection, we
considered all the crustal layers to be parallel down to
the crust mantle boundary such that the effect is simply
due to a contrast of 1.0 gm/cc where here we assumed a
mantle density of 3.4 gm/cc. Then, since all the deflec-
tions considered here are of long wavelength on the order
of a hundred kilometers, it is a good approximation to
calculate the gravity effect at the surface due to this
deflection by the infinite flat slab equation (Walcott,
1976) given by

$$g_w = 2\pi Gw(\rho_3 - \rho_2) ,$$

where w represents the displacement given by Equations
7, 8, 10, 11 or 12 depending on the model and horizontal
position being considered and g, ρ_2 and ρ_3 are the same
as defined earlier.

APPLICATION OF METHOD AND RESULTS

The application of this method to the Necker Ridge was done in the same manner as used by Watts and Cochran (1974) where the free-air anomalies were used to determine the effective flexural rigidity. In this way, the errors involved when using topographic relief to match the flexure are eliminated since tectonic activity and erosion both can alter the sea floor.

In determining the loads to be used for modeling the ridge, the observed topography was broken up into a number of columns as shown in Figure 16. Here the base line used represents the mean undisturbed sea floor for the adjacent area and the density of the load was taken in contrast to sea water. In calculating the load using the basement topography, the same scheme was used, as shown in Figure 17, where here the base line represents the mean basement level for the adjacent area. For this case, however, the most rigorous model would be to contrast the load density with sea water for that portion of the load projecting above the sea floor and contrast it with the sediment layer for that portion lying below the sea floor, within the sediments. In studying this model it was found that, for the size of load and thickness of sediment in this study, if we cal-culate the entire load by contrasting its density with sea water instead of breaking it up into the above two cases the error involved reaches a maximum of only (3.23$\pm$0.78) mgal. Since this error is within the accuracy of the

55

Figure 16. Observed topographic profiles (including
sediments) with their corresponding load
configurations used in calculating the de-
flection of the lithosphere.

TOPOGRAPHIC MODELS

57
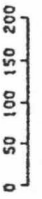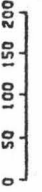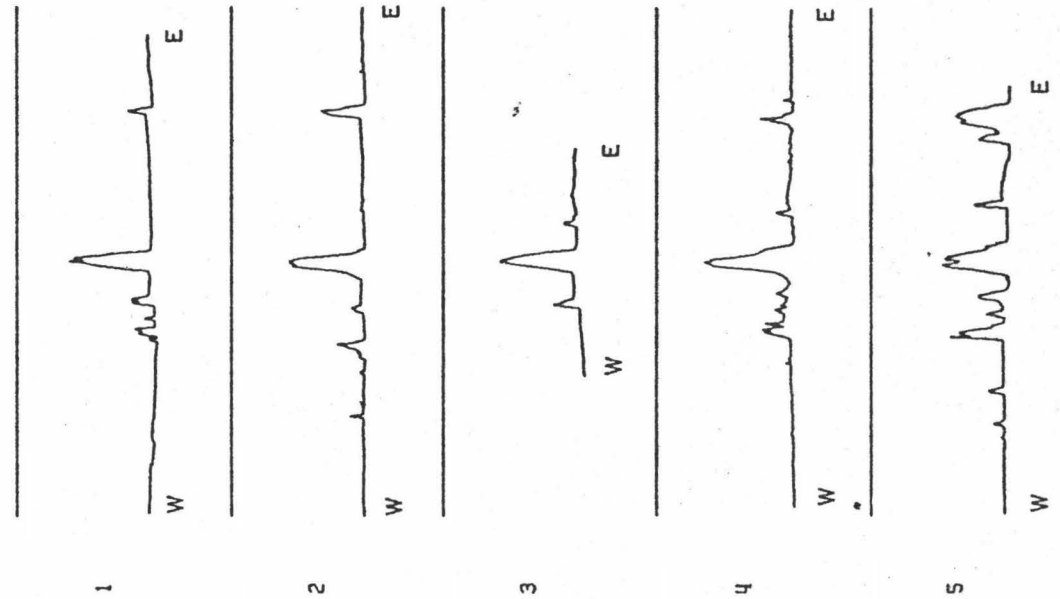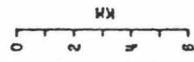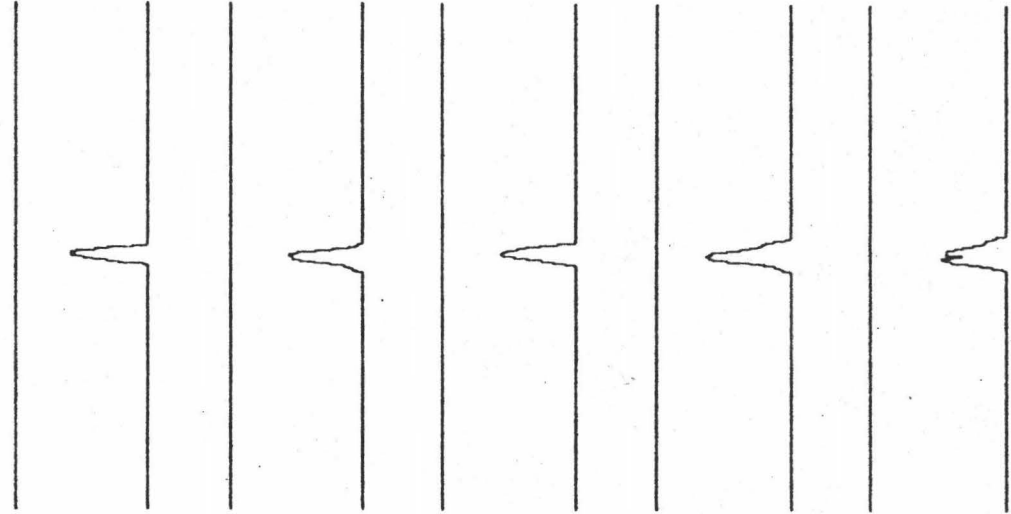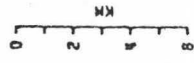
Figure 17. Basement topographic profiles with their
corresponding load configurations used in
calculating the deflection of the litho-
sphere.

TOPOGRAPHIC MODELS
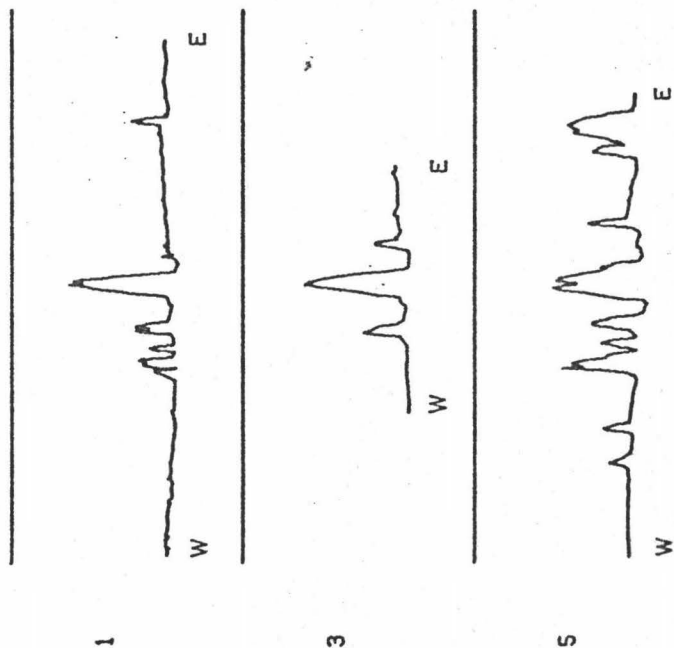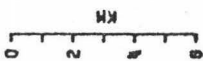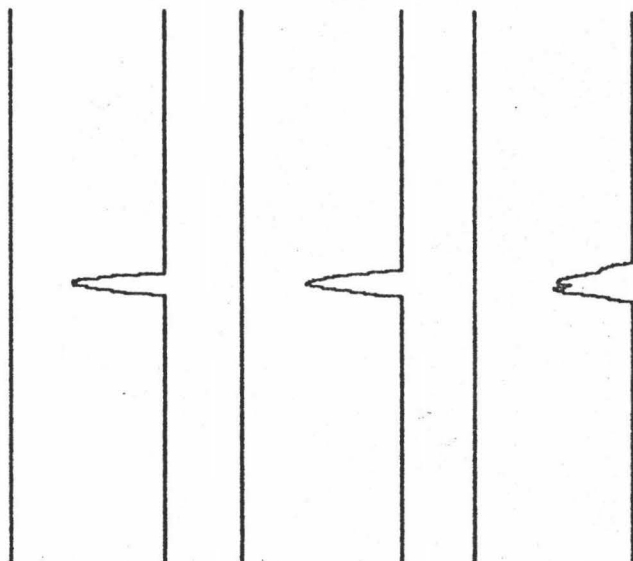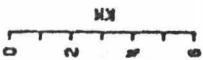
observed data, the loads here were calculated strictly in contrast to the sea water as with the observed topography case, thereby reducing the amount of modeling required. Then to obtain the total deflection, the deflection for each column was calculated and they were all summed using the principal of superposition as discussed earlier.

From the calculated deflection and observed topography, the corresponding gravity effect was computed and then compared with the observed free-air anomaly. This method was repeated several times for a number of different values of the effective flexural rigidity for each profile using the densities given in Table 3. The effective flexural rigidity which fit best was defined as the one which produced the minimum error between the calculated and observed free-air anomaly (hereafter called the best fit effective flexural rigidity). This error was defined as the square root of the average of the squares of the difference between the computed and observed gravity values.

In this study, deflection models were made for the data both before and after the sediment was corrected for in order to determine if it would have any effect on the determination of the best fit effective flexural rigidity. The computed gravity effect for those models fitting the data best are given in Figures 18 and 19 superposed on the observed gravity curves. The results show quite good correlation with the observed data where, from the calculated

60

Figure 18. Theoretical gravity effect of the best fit
effective flexural rigidity models superposed
on the observed free-air anomalies for both
the continuous plate model (Model I) and the
fractured plate model (Model II). The flexural
rigidities used here are given in Table 5.

MODEL I   MODEL II
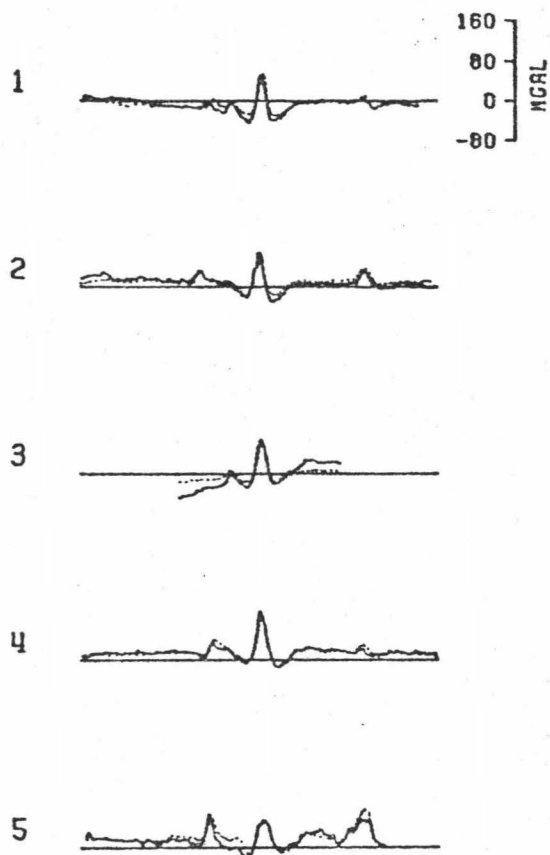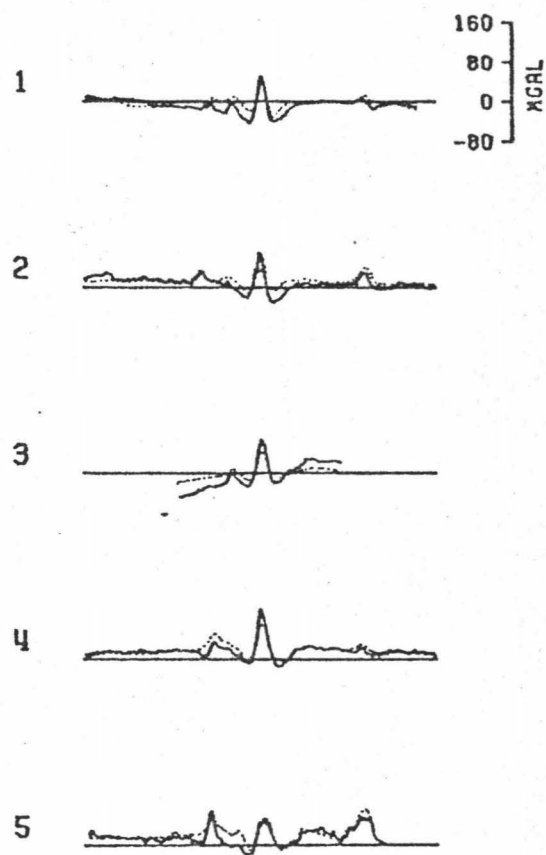
Figure 19. Theoretical gravity effect of the best fit
effective flexural rigidity models superposed
on the corrected free-air anomalies (with the
sediment effect removed). The flexural
rigidities used here are given in Table 5.

63
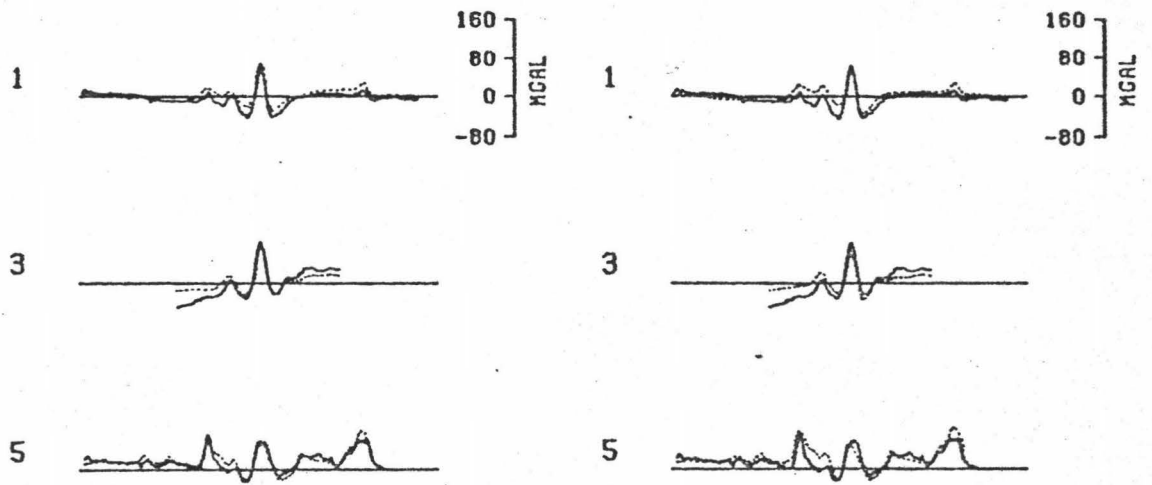
TABLE 5

SUMMARY OF BEST FIT PARAMETERS OBTAINED FOR A DENSITY OF 2.4 GM/CC

PROFILE	MODEL I				MODEL II			
	$D \times 10^{28}$ DYNE-CM		Y_{MAX} (KM)		$D \times 10^{28}$ DYNE-CM		Y_{MAX} (KM)	
	OBS	CORR	OBS	CORR	OBS	CORR	OBS	CORR
1	2.0	2.0	0.92	1.08	9.0	10.0	1.66	1.92
2	1.0		1.16		9.0		2.35	
3	5.0	6.0	0.77	0.96	20.0	30.0	1.58	1.92
4	5.0		1.03		40.0		1.70	
5	4.0	5.0	0.97	1.10	20.0	20.0	1.40	1.60
AVERAGE	3.4	4.33	0.97	1.05	19.6	20.0	1.74	1.81
	±1.82	±2.08	±0.14	±0.08	±12.66	±10.0	±0.36	±0.18

D = BEST FIT EFFECTIVE FLEXURAL RIGIDITY   OBS = OBSERVED DATA WITHOUT SEDIMENT REMOVED

Y_{MAX} = MAXIMUM DEFLECTION   CORR = OBSERVED DATA WITH SEDIMENT REMOVED

models, we can see that the best fit represents an average
fit of both the amplitude and wavelength of the anomaly.
In this way, the calculated models will more truly repre-
sent the overall subsurface structure instead of just a
small portion of it.

The major differences between the calculated and ob-
served anomalies lie in the areas of short-wavelength
gravity variations. These variations in turn can be cor-
related with changes in topography which flank the ridge,
where, due to their being three-dimensional features,
were not accounted for in the deflection equation. Profile
3 has a further discrepancy which, as described earlier,
represents a regional gradient due to its strike relative
to that of the Hawaiian Ridge.

A summary of the computed effective flexural rigidi-
ties used in Figures 18 and 19 is given in Table 5 where
comparison of the models before and after the sediment
correction show an average increase in the best fit effec-
tive flexural rigidity of about 1×10^{28} dyne-cm for both
the continuous plate and fractured plate models. It can
also be seen that the best fit effective flexural rigidity
increases slightly from the northern profiles to those in
the south with an average value over the entire ridge of
$(4.33 \pm 2.08) \times 10^{28}$ dyne-cm for the continuous model and
$(2.0 \pm 1.0) \times 10^{29}$ dyne-cm for the fractured model.

In order to determine how sensitive the computed

models are to a change in load densities the above procedure

was repeated for a range of densities from 2.3 to 2.7 gm/cc.

A summary of the best fit effective flexural rigidities

is given in Table 6. Here it can be seen that a change in

the load density by 0.2 gm/cc can change the effective

flexural rigidity by as much as 20%.

Other studies made in this area have also determined

an effective flexural rigidity for the lithosphere. One

study, by Watts and Cochran (1974) obtained an average

effective flexural rigidity under the entire Hawaiian -

Emperor Seamount Chain of 5 x 10^{29} dyne-cm for the continuous

model and 2 x 10^{30} dyne-cm for the fractured model. Another

study, by Walcott (1970a, 1976) found the effective flexural

rigidity around the Island of Hawaii to be 7.6 x 10^{29} dyne-cm

for the continuous model and 1.4 x 10^{31} dyne-cm for the

fractured model. Thus both of these studies have determined

values an order of magnitude greater than those found in

this study. Since a simple change in the load parameters

cannot produce this kind of change, the lithosphere was

next modeled as a viscoelastic body as described earlier.

In using this model, a relaxation time of 10^5 years

was used as proposed by Walcott, with a Young's Modulus

of E = 10^{12} dyne cm^{-2} and a Poisson's ratio of $\sigma = 0.5$

producing an effective viscosity of the lithosphere of

$\eta = 4.2$ x 10^{24} poise. For this study, we chose Poisson's

ratio to be 0.5 so as to be the limiting case, due to the

TABLE 6

BEST FIT EFFECTIVE FLEXURAL RIGIDITY FOR VARYING DENSITY

DENSITY (GM/CC)	MODEL I D x 10^{28} DYNE-CM						MODEL II D x 10^{28} DYNE-CM				
	2.3	2.4	2.5	2.6	2.7		2.3	2.4	2.5	2.6	2.7
PROFILE											
1 OBS	2.0	2.0	1.0	0.9	0.8		10.0	9.0	7.0	6.0	5.0
1 CORR	2.0	2.0	2.0	1.0	0.9		10.0	10.0	9.0	7.0	6.0
2 OBS	2.0	1.0	0.9	0.7	0.5		10.0	9.0	7.0	5.0	4.0
3 OBS	6.0	5.0	4.0	4.0	3.0		30.0	20.0	20.0	20.0	20.0
3 CORR	7.0	6.0	5.0	5.0	4.0		40.0	30.0	30.0	20.0	20.0
4 OBS	6.0	5.0	4.0	3.0	3.0'		40.0	40.0	30.0	30.0	20.0
5 OBS	5.0	4.0	3.0	3.0	2.0		20.0	20.0	10.0	10.0	8.0
5 CORR	6.0	5.0	4.0	4.0	3.0		30.0	20.0	20.0	10.0	9.0

OBS = OBSERVED DATA WITHOUT SEDIMENT REMOVED

CORR = OBSERVED DATA WITH SEDIMENT REMOVED

assumed viscous properties of the lithosphere, although in
reality it should be lower than this. The age of the Necker
Ridge has been found to lie between given limits, but no
specific age has yet been determined. The minimum age
has been found by Ozima to be at least 60 my using K-Ar
data (Clague, 1974) and the maximum age has been set at the
age of the sea floor of 95 ± 10 my (R. Moberly, pers. comm.).
One dredging was taken in the area at latitude 23.6°N and
longitude 165.5°W which was found to be 77.6 ± 1.7 my
(Clague, 1974) using K-Ar dating.

Next, in order to determine how the effective flexural
rigidity changes with respect to time, we need to match the
viscoelastic deflection (Figure 15) assuming an elastic
model. In doing this, our result will depend on whether
the amplitude or wavelength is matched as well as on which
of the two elastic models is used.

For this study, we matched both the wavelength and
the amplitude of the viscoelastic model, assuming first an
elastic continuous plate model, and then an elastic frac-
tured plate model.

First, consider the viscoelastic deflections calcula-
ted earlier in Figure 15. Using an elastic continuous plate
model, the deflections which match the viscoelastic wave-
length are plotted in Figure 20 while those which match
the amplitudes are plotted in Figure 21. Both sets of
curves have been normalized to the initial elastic deflec-

69

Figure 20. Continuous elastic plate deflections which
match the wavelengths produced by the same
load when applied to a viscoelastic plate,
(Figure 15).

Figure 21. Continuous elastic plate deflections which
match the amplitudes produced by the same
load when applied to a viscoelastic plate
(Figure 15).
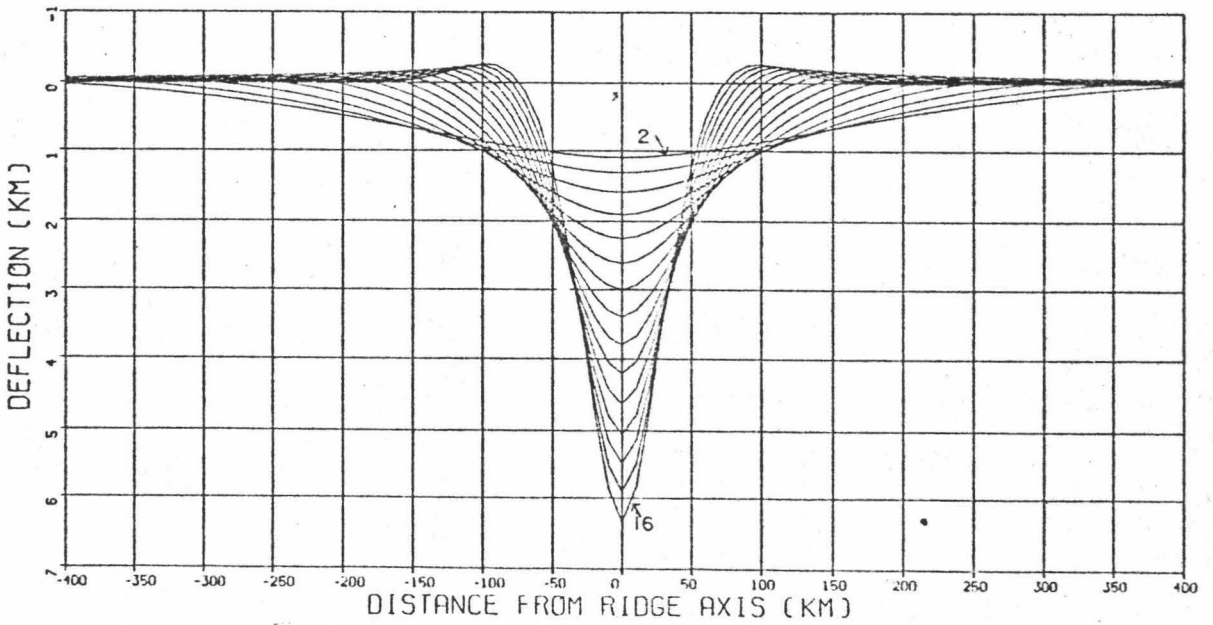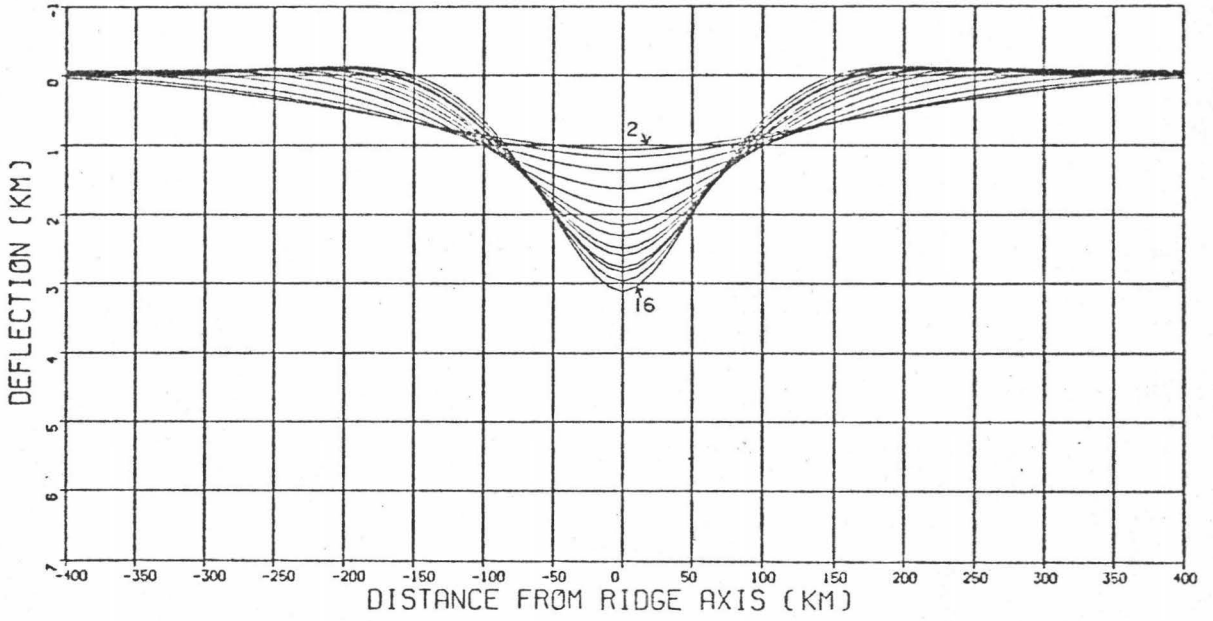
tion. It can be seen here that for the age of the Necker Ridge (60-95 my) the best overall fit will lie closer to the amplitude matched curves rather than the wavelength matched curves.

In order to compare these predicted values for the effective flexural rigidity with those calculated earlier, a number of different matches of both the wavelength and amplitude were run by changing the instantaneous effective flexural rigidity, D_0. The values of D_0 chosen corresponded to effective plate thicknesses of 30-80 km and are plotted in Figures 22 through 27. In calculating these curves the same parameters were used as given in Table 4 with the only change being for the D_0 term.

Since the above curves represent how the predicted effective flexural rigidity will change with time only for the continuous elastic plate model, the same method was then applied matching the wavelengths and amplitudes using a fractured elastic plate model. These curves are given in Figures 28 through 31 and cover a range of effective lithospheric thicknesses of 10-40 km.

From the predicted curves, it can be seen that an effective thickness of between 40-70 km will explain the values determined for Model I (the continuous elastic plate) while an effective thickness of between 20-35 km is needed to explain those for Model II (the fractured elastic plate).

72

Figure 22. Change in effective flexural rigidity with
time for a continuous viscoelastic plate of
thickness 30 km modeled as a continuous elastic
plate. The circle represents the average
best fit effective flexural rigidity as
found in this study for a continuous plate
model under the Necker Ridge.

CHANGE IN D FOR T=30 KM

74
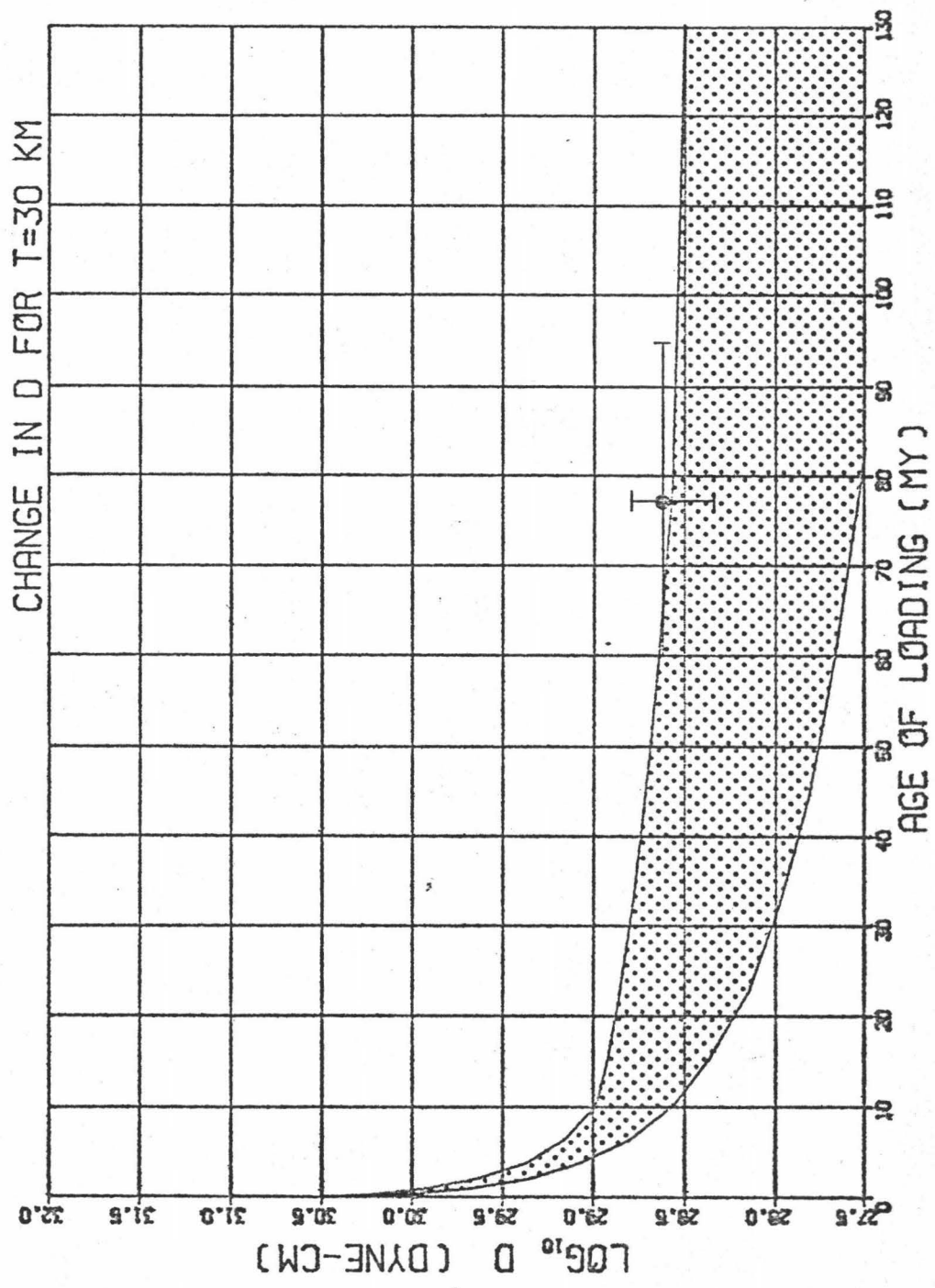
Figure 23. Same as Figure 22 for a thickness of 40 km.

CHANGE IN D FOR T=40 KM
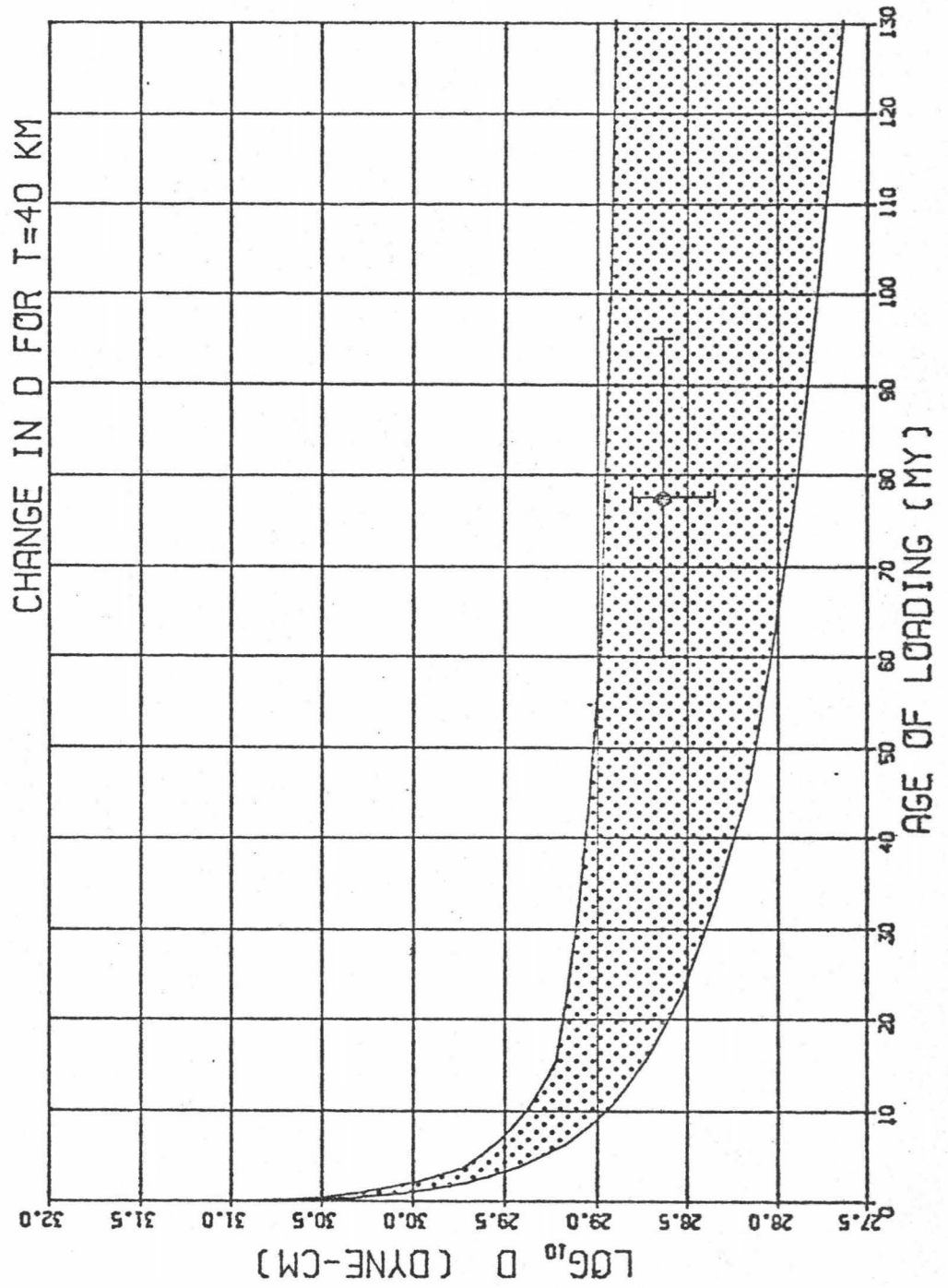
Figure 24. Same as Figure 22 for a thickness of 50 km.

CHANGE IN D FOR T=50 KM
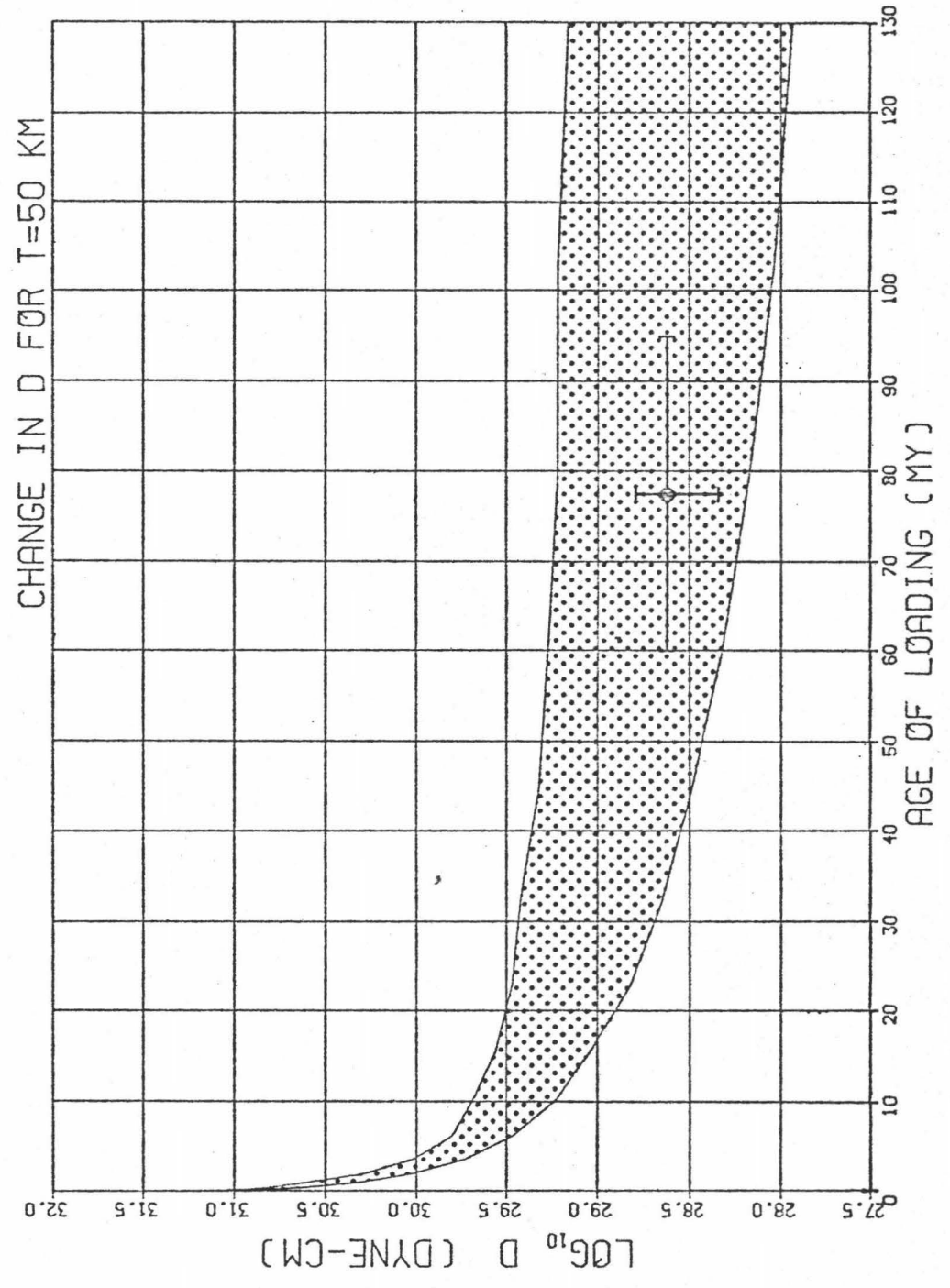
Figure 25.   Same as Figure 22 for a thickness of 60 km.

CHANGE IN D FOR T=60 KM
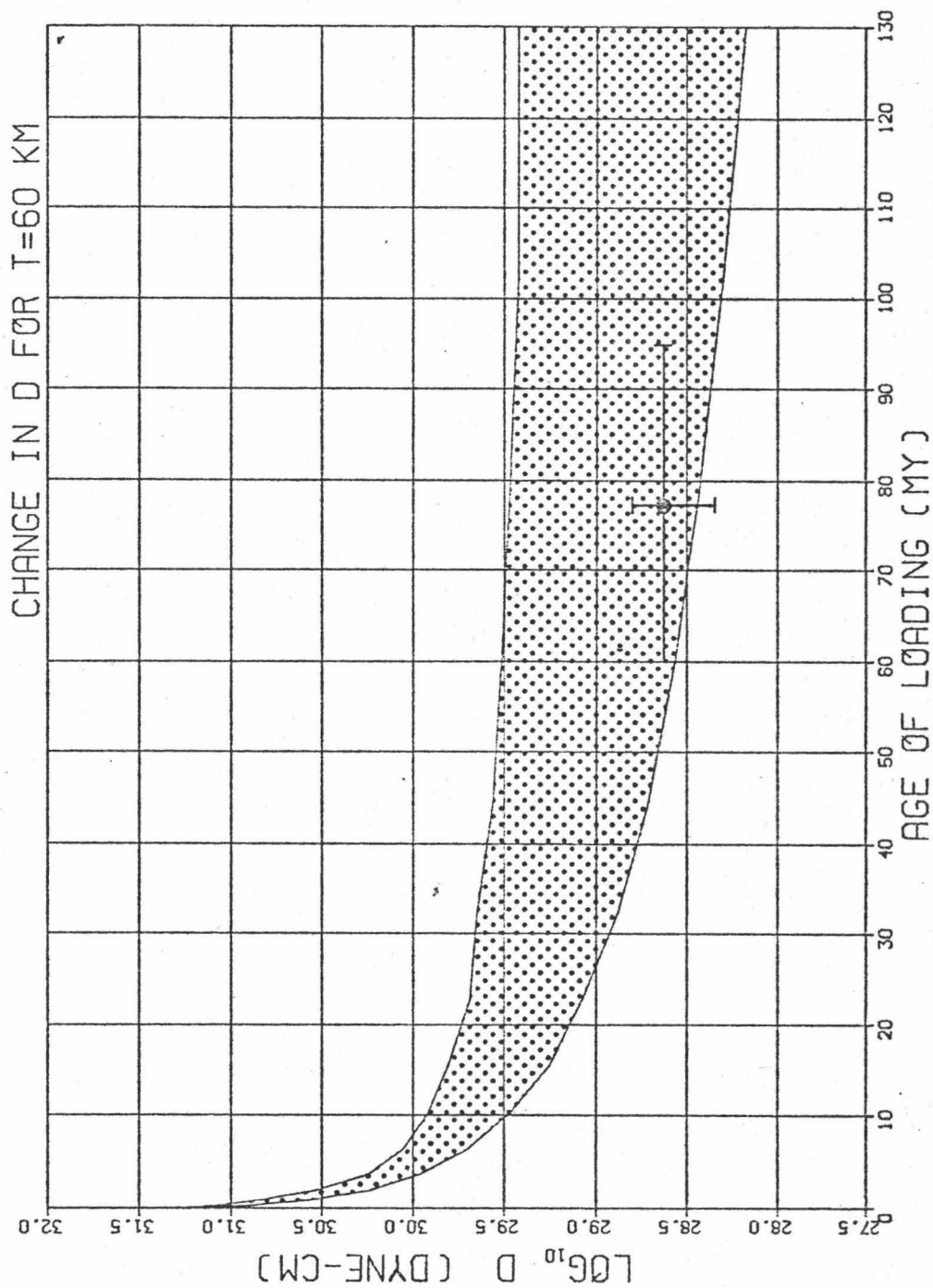
Figure 26. Same as Figure 22 for a thickness of 70 km.

CHANGE IN D FOR T=70 KM

82
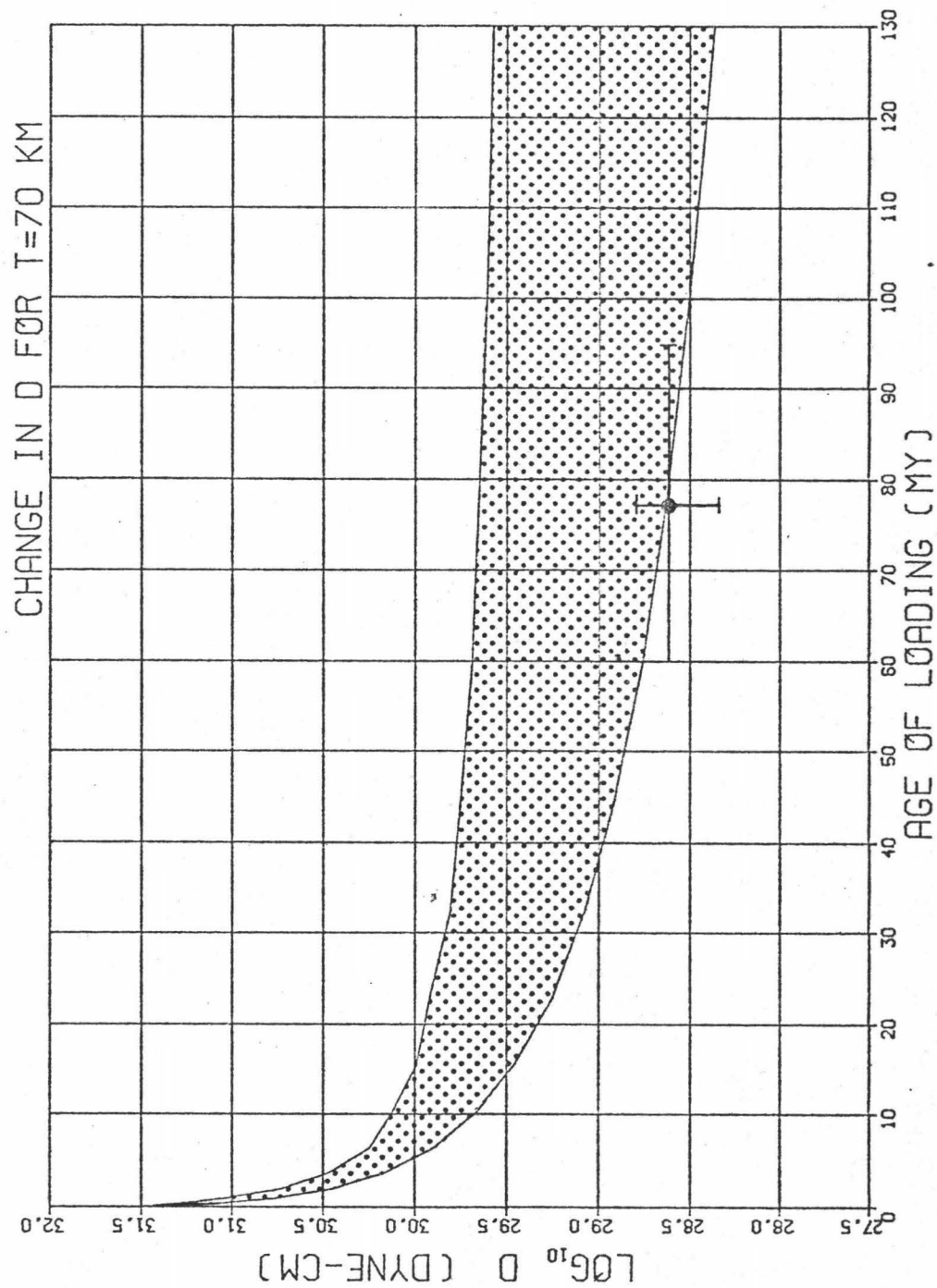
Figure 27. Same as Figure 22 for a thickness of 80 km.

CHANGE IN D FOR T=80 KM.

84
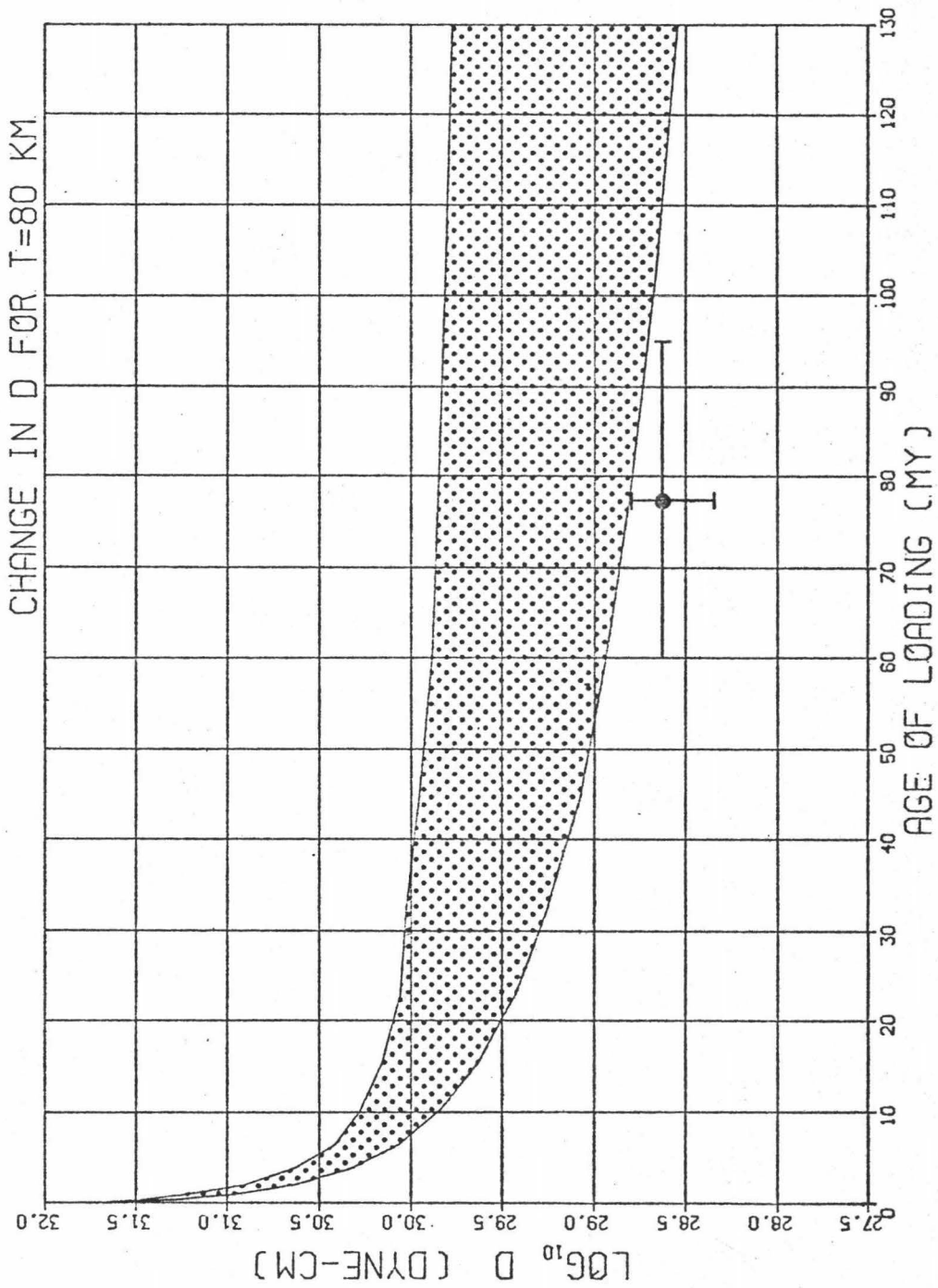
Figure 28.   Change in the effective flexural rigidity
with time for a continuous viscoelastic
plate of thickness 10 km modeled as a frac-
tured elastic plate. The square represents
the average best fit effective flexural
rigidity as found in this study for a frac-
tured plate model under the Necker Ridge.

CHANGE IN D FOR T=10 KM

85
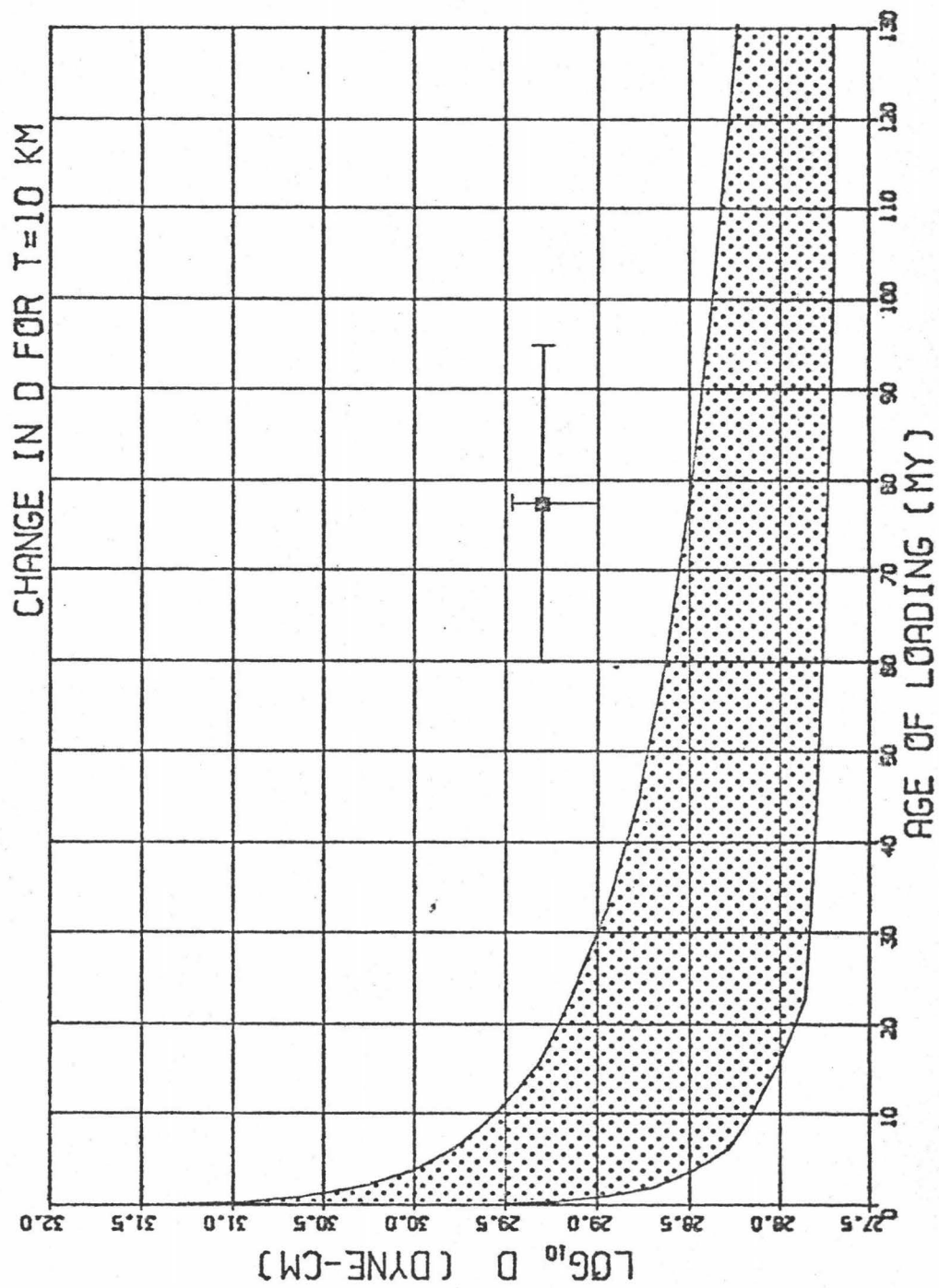
Figure 29. Same as Figure 28 for a thickness of 20 km.

CHANGE IN D FOR T=20 KM

88
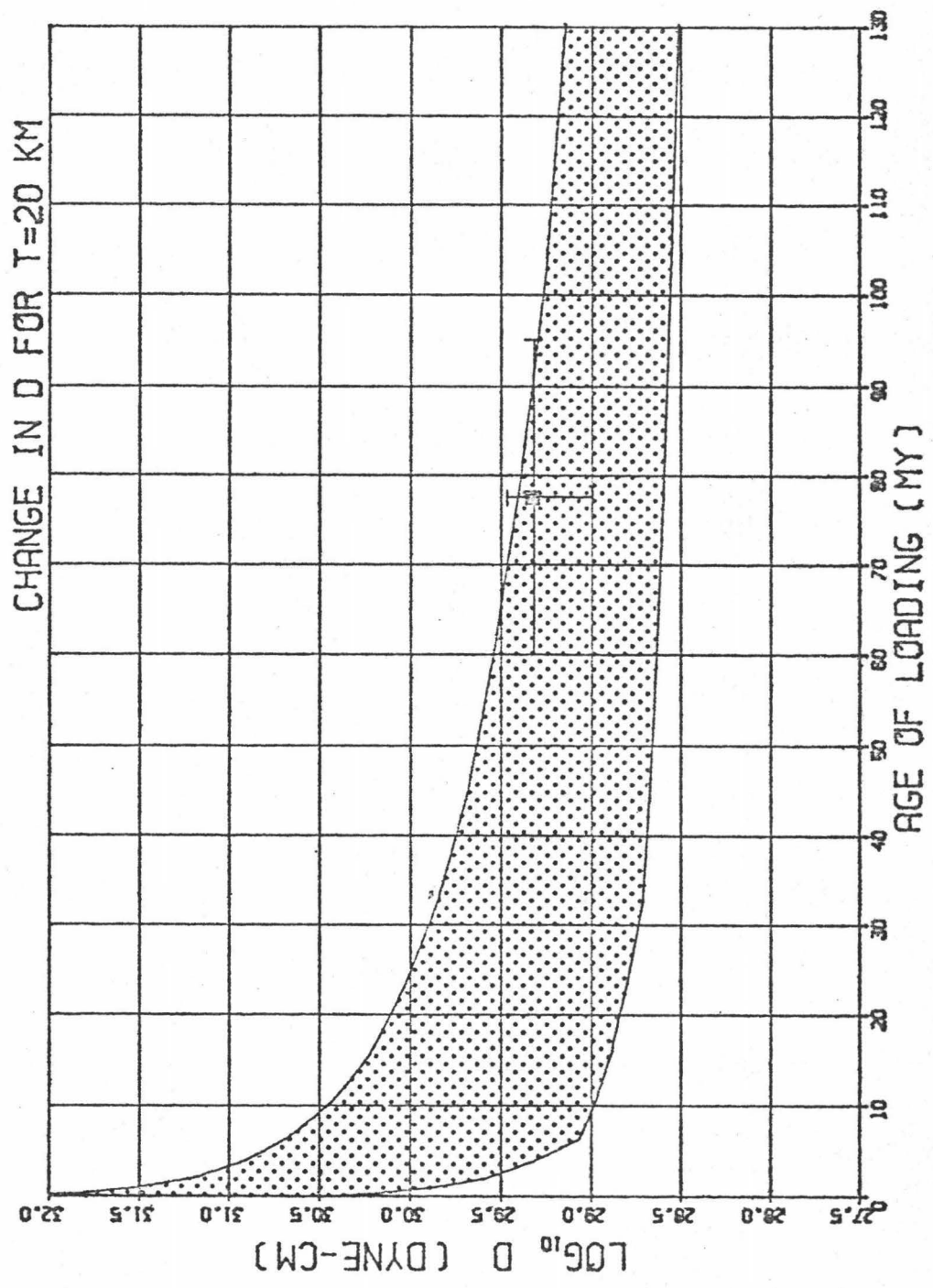
Figure 30. Same as Figure 28 for a thickness of 30 km.

CHANGE IN D FOR T=30 KM

89
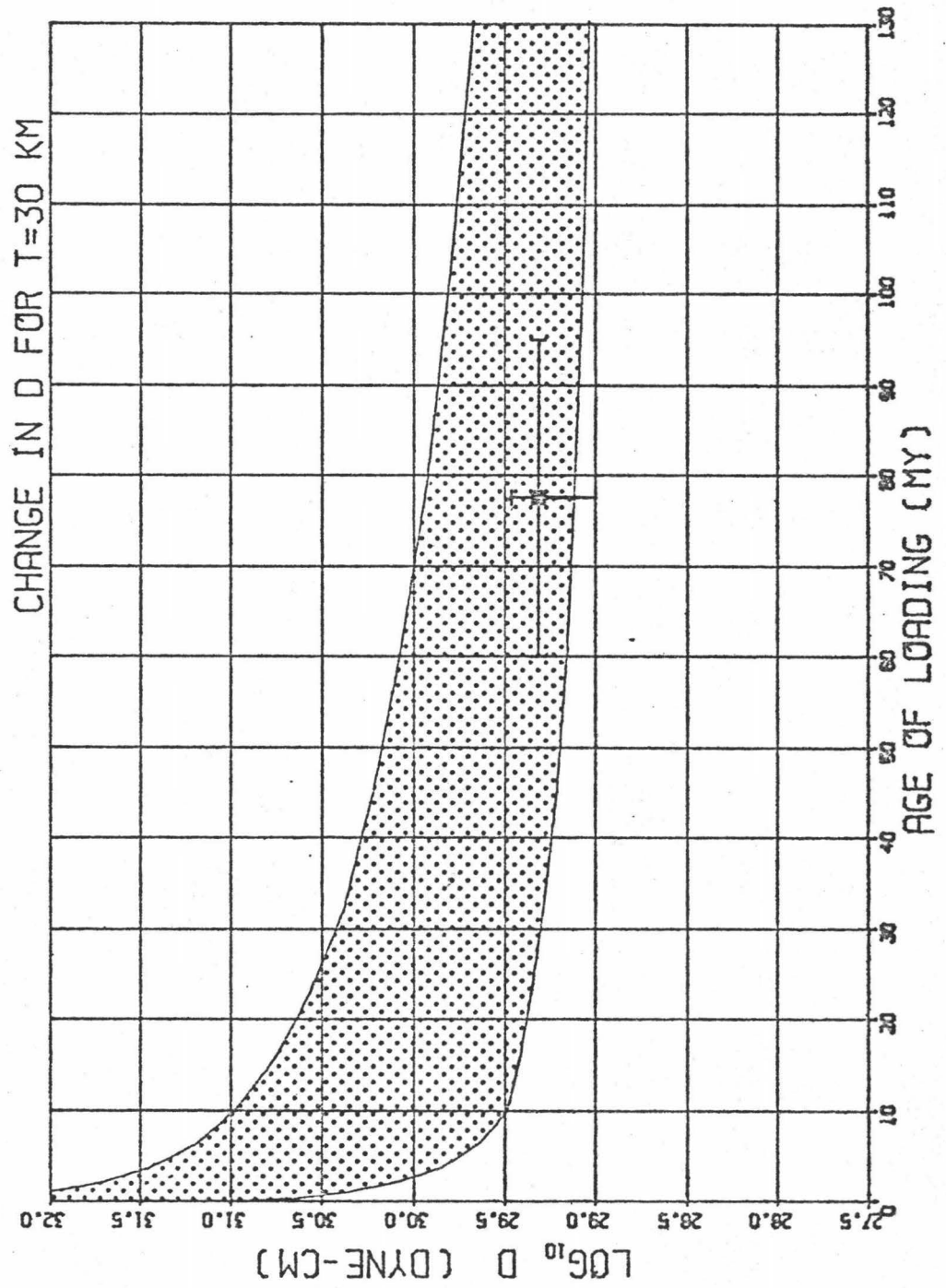
Figure 31. Same as Figure 28 for a thickness of 40 km.

CHANGE IN D FOR T=40 KM

LOG$_{10}$ D (DYNE-CM)

AGE OF LOADING (MY)
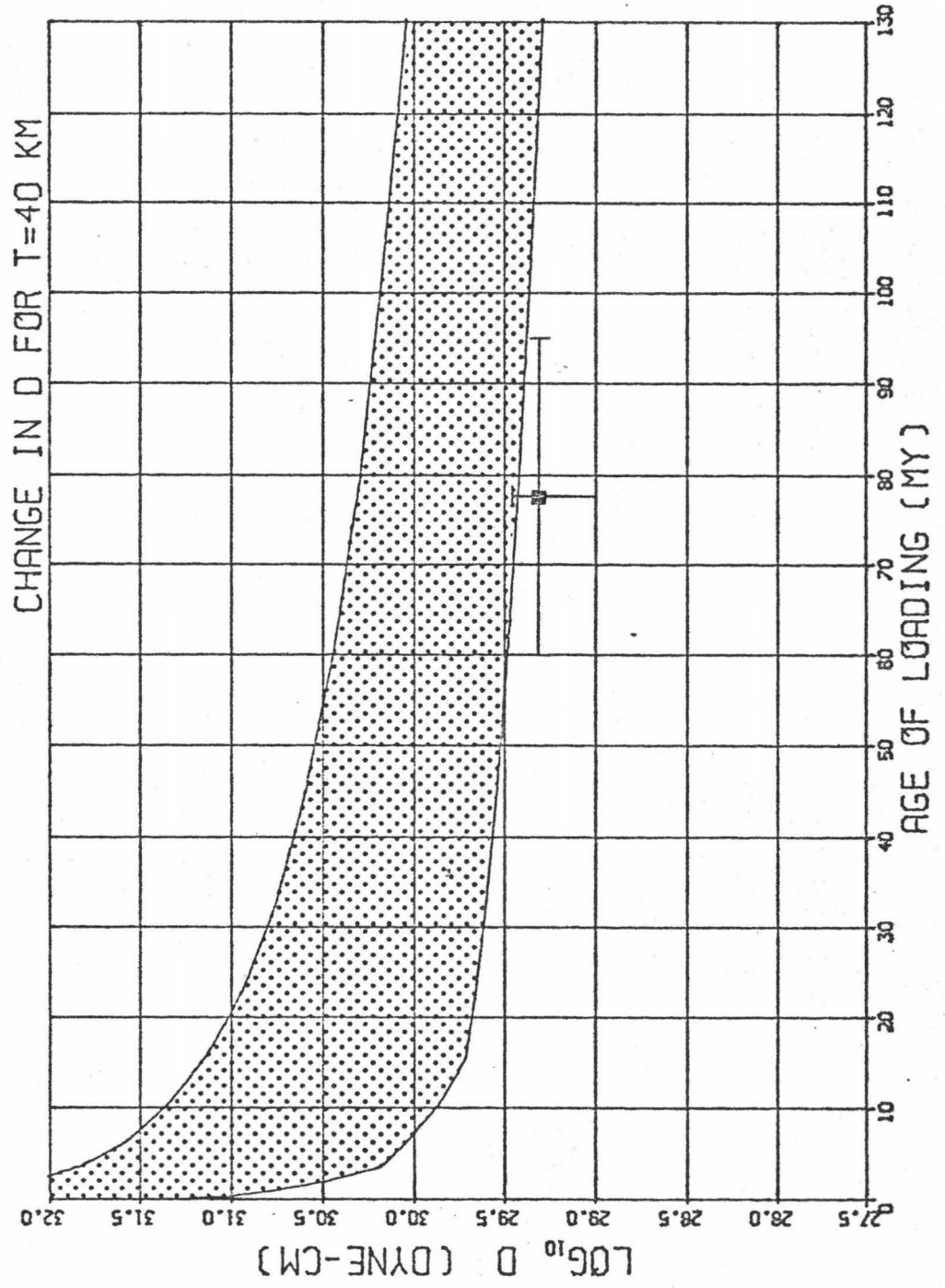
DISCUSSION

To summarize our findings up to this point, we have shown the following:

1) The average density of the Necker Ridge is about 2.4 gm/cc.

2) When modeling the lithosphere as an elastic plate, the best fit effective flexural rigidity is:

   a) for a continuous sheet : $(4.33 \pm 2.08) \times 10^{28}$ dyne-cm.

   b) for a fractured sheet : $(2.0 \pm 1.0) \times 10^{29}$ dyne-cm.

3) When removing the effect of the local sediments, it was found that:

   a) their gravitational attraction should be calculated using their true density.

   b) the increased load height need only be considered as an extension of the rest of the load, taking its density in contrast with water and not the sediments.

4) If the sediment effect is not removed, there will be an error on the order of 1.0×10^{28} dyne-cm in the calculated best fit effective flexural rigidity.

5) A change in load density by 0.2 gm/cc can cause a change in the best fit effective flexural rigidity by as much as 20%.

6) When modeling the lithosphere as a viscoelastic body, the required thickness needed to explain the modeled values for the elastic plate models are:

   a) for the continuous plate: 40 - 70 km.

   b) for the fractured plate: 20 - 35 km.

If we first consider the lithosphere as an elastic plate, then upon substitution of the above modeled values

for the best fit effective flexural rigidity into Equation
14, we can obtain the effective thickness of the lithosphere
which is necessary to explain the observed results. In
doing this for the continuous elastic plate model we get
a thickness of 7.86 km, while for the fractured elastic
plate model we get 13.1 km. It should be noted that the
above thicknesses represent strictly effective thicknesses
so that a lower value would be expected with respect to
the true lithospheric thickness. But even with this con-
sideration, both modeled thicknesses are still quite thin.

In a similar study by Watts and Cochran (1974), the
same models were run near Nihoa Island which lies within
300 km of Necker Ridge. This study found best fit effec-
tive flexural rigidities of 4.0 x 10^{29} dyne-cm for the
continuous elastic plate model and 1.0 x 10^{30} dyne-cm for
the fractured elastic plate model. Substituting these
values into Equation 14 to obtain the plate thicknesses
yields 16.5 km and 22.4 km for the continuous and frac-
tured models respectively. Although these values are still
quite low, a more important aspect to notice is that the
lithosphere must thicken by approximately 9 km for both
models if the elastic lithospheric case is to hold.

No explanation has been found which adequately explains
the required thin lithosphere as well as the rapid change
in thickness as calculated above. It is therefore concluded

here that an elastic lithospheric model is not a valid one.

In modeling the lithosphere as a viscoelastic body, it has been shown that, depending on how we match the viscoelastic deflection, a given range of thicknesses can be found which will explain the observed data. If we first consider the viscoelastic lithosphere modeled as a fractured elastic plate, then the required thickness needed to explain the observed data must lie within the range 20-35 km. Although this range is larger than the values determined using the elastic case, it is still quite low, requiring a very thin lithosphere.

If we are to consider the lithosphere as the relatively rigid upper portion of the earth underlain by a relatively fluid substratum then it seems valid to assume that no earthquake foci will occur below the lithosphere, within the asthenosphere. In a study by Eaton and Murata (1960), it was found that for the Hawaiian Islands, the deepest earthquakes observed originated at a depth of about 60 km, that being the approximate lower limit. If we use this as an approximate upper limit for the base of the lithosphere, then upon subtracting the water depth, we get a minimum thickness on the order of 55 km. Therefore, using this value as an approximate thickness, we see that the above range of 20-35 km is still much lower than expected. On the other hand, if we consider the viscoelastic

lithosphere modeled as a continuous elastic plate, then our required thickness will lie within the range 40-70 km which does in fact seem reasonable as compared to the above predicted value. We therefore conclude that the lithosphere can be adequately modeled as a continuous visco-elastic body and described using continuous elastic plate theory allowing for a viscoelastic effect with time. It should further be noted that although this method does not determine an exact lithospheric thickness, it does determine a range of thicknesses which will explain the observed data. Also, as pointed out earlier, for loads of longer duration, the best overall fit will lie closer to the elastic amplitude fit of the viscoelastic deflection which, in effect, implies that the best fit will lie closer to the thicker portion of our range of calculated thicknesses. In this light, it seems that for the Necker Ridge area a viscoelastic lithosphere of thickness in the range of 50-70 km would seem to explain the observed data as well as the minimum thickness determined seismically.

We will now look at the results obtained by Watts and Cochran (1974) for their profile near Nihoa Island, where they matched the viscoelastic deflections using only the continuous elastic plate model and not the fractured elastic plate model. In their study, when using the continuous elastic plate to match the visco-

elastic deflections, they show that a plate thickness of 50 km is the minimum value which explains the observed results. They further show that a plate thickness of 75 km is too large to explain their results yielding an acceptable range of 50-70 km thickness which will explain their data.

This thickness range, being the same as that found for this study, strongly supports the idea that a visco-elastic lithospheric model is a good one. It further introduces the possibility that deflection studies, such as these, can be used to determine a range of lithospheric thicknesses for different areas.

We will next consider the overall results found by Watts and Cochran (1974) for the best fit effective flexural rigidities over the entire Hawaiian - Emperor Seamount Chain. From their results it is seen that the observed rigidities increase from the northernmost part of the Em-peror Seamounts down to the Hawaiian - Emperor Bend. The loads used to compute these rigidities are all fairly old, ranging from 58.5 my in the north to 45 my near the bend where, from Figures 22-27, these ages directly correlate with a thickening of the lithosphere. Therefore, to explain their results using a viscoelastic lithospheric model, the lithosphere is required to thicken from the northern Emperor Seamounts going south toward the Hawaiian - Emperor Bend.

In the same study, Watts and Cochran also looked at three profiles along the Hawaiian Chain, one of which has already been discussed. Another of these profiles, which lies further southeast of Necker Ridge, near the island of Oahu, was shown to require a lithospheric thickness of at the most, 50 km to fit the data. Their last profile, which was halfway between the Necker Ridge and the Hawaiian - Emperor Bend also required a thickness of about 50 km. Although there is no obvious trend here, with the exception of the last profile mentioned, there seems to be an indication that the lithosphere thickens as one goes from Hawaii toward the Hawaiian - Emperor Bend, recalling that for the Necker Ridge area a thickness of 50-70 km is needed to explain the data.

If we now consider how the age of the sea-floor varies over this area, we see that the youngest areas are at the northern end of the Emperor Seamounts and around the Island of Hawaii, while the oldest area is at the Hawaiian - Emperor Bend (Hilde, et al., 1976). This then draws a direct correlation between lithospheric age and thickness, where the older it is, the thicker it becomes. We conclude that: (1) the lithosphere can be modeled as a continuous viscoelastic plate overlying a fluid substratum; (2) deflection studies based on a continuous viscoelastic lithosphere can be used to determine effective plate thick-

nesses; (3) the effective plate thickness under the
Necker Ridge is between 50-70 km; and (4) the lithosphere
seems to thicken with age, although it is beyond the
scope of this study to determine any specific thicknesses
other than that for the Necker Ridge area.

APPENDIX

LOADING OF AN ELASTIC LITHOSPHERE

We shall consider here an elastic lithosphere rest-
ing on a substratum (asthenosphere) of negligible strength.
The following notation will be used:

H = thickness of the lithosphere
ρ_1 = density of load

ρ_2 = density of infilling material

ρ_3 = density of the asthenosphere

Consider first the bending of a long rectangular
plate, subjected to a transverse load which does not vary
along the length of the plate. In this way we can consider
the deflected surface of a portion of the plate, a consi-
derable distance from the ends of the plate, as cylindri-
cal where here we shall define the axis of the cylinder
as the y-axis (Figure 32).

To obtain the equation for the deflection of the
plate, we shall consider the plate to be of uniform thick-
ness H and shall take the xy plane as the middle plane of
the plate before loading (i.e., midway between the faces of
the plate) with the z-axis positive downward.

In setting up the problem like this, we need only
consider a small strip of unit width in order to analyze
the deflection. If we further assume the lithosphere as
being continuous, then we have the condition that there
will be no distortions in the cross-section of the strip

100

Figure 32. Lithospheric model used for this study. The
            model represents a rectangular plate subjec-
            ted to a line load along the y-axis.

Figure 33. Cross-section of the lithospheric model shown
            in Figure 32. The line NN' represents the
            neutral surface which undergoes no longitudi-
            nal strain during deformation.
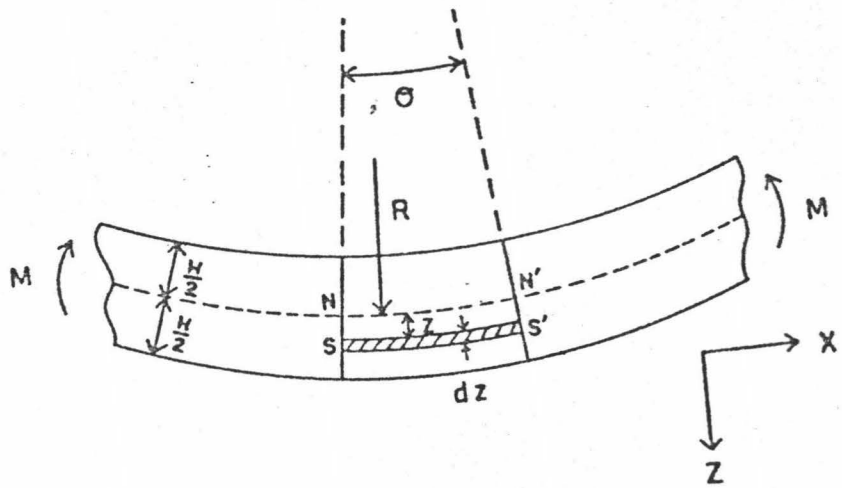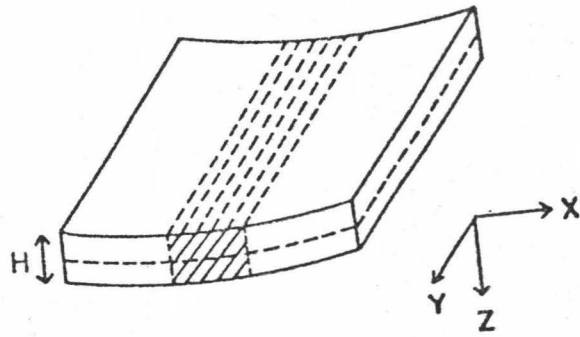
during bending. Our cross-section is shown in Figure 33 where it can be seen that as the plate is loaded, the upper portion will undergo compression while the lower portion undergoes tension. Thus we have a surface which will undergo no longitudinal strain, defined as the neutral surface, as shown by the line NN' in Figure 33. If we define the radius of curvature of the plate, R, as the distance to the neutral surface, then we can derive a convenient expression for the strain by defining it as the change in length per unit length. Thus we can write

$$\varepsilon_{xx} = \frac{\Delta NN'}{NN'} = \frac{SS' - NN'}{NN'} = \frac{(R+Z) - R}{R} = \frac{Z}{R} \quad . \tag{A1}$$

Consider next Hooke's Law for an isotropic solid given by

$$\varepsilon_{ij} = \frac{1 + \sigma}{E} \sigma_{ij} - \frac{\sigma}{E} \delta_{ij} \sigma_{kk} , \tag{A2}$$

where ε_{ij} = strain

σ_{ij} = stress

σ = Poisson's ratio

E = Young's Modulus.

From our assumption of no distortion occurring in the cross-section we have the condition that $\varepsilon_{yy} = 0$ where, from Equation (A2), we get $\sigma_{yy} = \sigma\sigma_{xx}$ or upon substitution again into Equation (A2) yields

$$\sigma_{xx} = \frac{E}{1 - \sigma^2} \varepsilon_{xx} \tag{A3}$$

which becomes after substitution of Equation (A1)

$$\sigma_{xx} = \frac{EZ}{(1 - \sigma^2)R} \tag{A4}$$

It is easy to show through a study of the curvature of the fiber NN' that for small deflections ($\frac{w}{R} = 0$) we can write

$$-\frac{d^2w}{dx^2} = \frac{1}{R} \tag{A5}$$

with which (A4) becomes

$$\sigma_{xx} = \frac{-EZ}{1-\sigma^2} \frac{d^2w}{dx^2} \quad . \tag{A6}$$

Now consider the force distributed over just the shaded portion of Figure 32 in the xz plane. This force can be written as $\sigma_{xx}dz$ whereby the internal couple (bending moment) about the y-axis associated with the bending in the xz plane is given by $(\sigma_{xx}dz)z$. Summing up all the moments on the complete cross-section and substituting in (A6) yields the total external couple, M :

$$M = \int_{-H/2}^{H/2} Z\sigma_{xx}dZ = -D \frac{d^2w}{dx^2} , \tag{A7}$$

where $\qquad D = E \times H^3 / [12 \times (1 - \sigma^2)] \tag{A8}$

is called the effective flexural rigidity of the plate.

In order to develop the equilibrium equations, we will define the shearing force, Q, acting on our cross-section as the algebraic sum of all the external forces applied to the cross-section and the bending moment, M, as the sum of all the external couples applied to the

cross-section. If we define our plate as being subjected to a vertical force, F, then there will be, due to the resultant deflection, a continuously distributed reaction force (Buoyancy force) in the asthenosphere directed upward and opposing the deflection. This force will, in turn, be directly proportional to the deflection, and so can be defined as p = kw for some given point.

Now consider just an infinitely small element of our cross-section, as shown in Figure 34. In this case, $p = g\rho_3 w$ represents the resultant force per unit length due to the deflection, F represents the net vertical external force per unit length being applied to the plate, Q represents the shearing force (defined as positive upward) and M represents the bending moment (defined as positive in the clockwise direction).

The equation for the equilibrium of the vertical forces then becomes

$$Q - (Q + dQ) + pdx = Fdx = 0 ,$$

or

$$\frac{dQ}{dx} = p - F = g\rho_3 w - F \qquad (A9)$$

and similarly, the equation for the equilibrium of the moments about the y-axis becomes

$$dM - Qdx = 0 ,$$

or

$$Q = \frac{dM}{dx} \qquad (A10)$$

105

Figure 34. Cross-section of our lithospheric model,
            showing the direction of forces acting
            upon an infinitely small element of it.
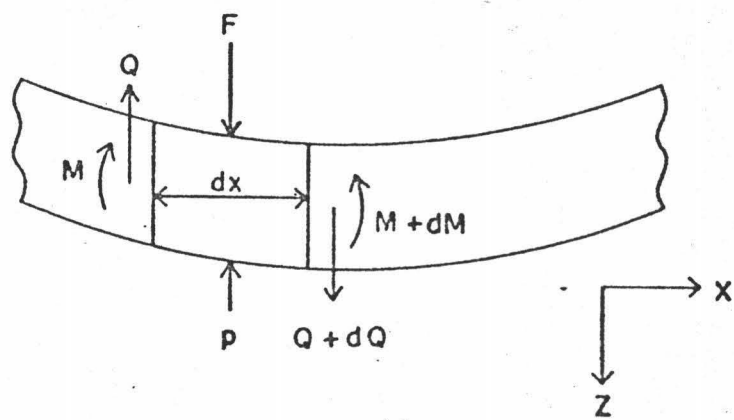
where, if we combine (A9) and (A10) we get

$$\frac{d^2M}{dx^2} = g\rho_3 w - F$$

and using our relation for M given in (A7) we get

$$D\frac{d^4w}{dx^4} + g\rho_3 w = F \; . \tag{A11}$$

In our particular case we shall divide the applied force F into two components:

1) an applied load such as a ridge or a continent impinging on a downgoing slab given as "P"; and

2) a downward force applied to the plate by any material infilling the deflection given by "$g\rho_2 w$".

Thus our deflection equation becomes

$$D\frac{d^4w}{dx^4} + g\rho_3 w = g\rho_2 w + P \; ,$$

or more conveniently

$$D\frac{d^4w}{dx^4} + (\rho_3 - \rho_2)gw_, = P \; . \tag{A12}$$

BIBLIOGRAPHY

Barrell, J., 1914a. The Strength of the Earth's Crust, No. 5, J. Geol., v. 22, pp. 441-468.

_____, 1914b. The Strength of the Earth's Crust, No. 6, J. Geol., v. 22, pp. 537-555.

_____,1915. The Strength of the Earth's Crust, No. 8, J. Geol., v. 23, pp. 425-443.

Chase, T. E., et al., 1970. Bathymetry of the North Pacific, Scripps Institution of Oceanography and Institute of Marine Resources.

Clague, D. A., 1974. The Hawaiian-Emperor Seamount Chain: Its Origin, Petrology, and Implications for Plate Tectonics, PhD. Thesis. Univ. of Calif. at San Diego.

Cochran, J. R., 1973. Gravity and Magnetic Investigations in the Guiana Basin, Western Equatorial Atlantic, Geol. Soc. Am. Bull., v. 84, pp. 3249-3267.

Deffeyes, K. S., 1972. Plume Convection with an Upper-Mantle Temperature Inversion, Nature, v. 240, pp. 539-544.

Dietz, R. S. and Menard, H. W., 1953. Hawaiian Swell, Deep and Arch and Subsidence of the Hawaiian Islands, J. Geol., v. 61, pp. 99-113.

Den, N., et al., 1969. Seismic-Refraction Measurements in the Northwest Pacific Basin, J. Geophys. Res., v. 74, pp. 1421-1434.

Eaton, J. P., and Murata, K. J., 1960. How Volcanoes Grow, Science, v. 132, pp. 925-938.

Furumoto, A. S., et al., 1971. Seismic Refraction Surveys along the Hawaiian Ridge, Kauai to Midway Island, Bull. Seismol. Soc. of Am., v. 61, pp. 147-166.

_____, 1968. Variation in the Thickness of the Crust in the Hawaiian Archipelago, Geophys. Monograph 12, Am. Geophys. Union, Wash. D. C., pp. 94-111.

Furumoto, A. S., and Woollard, G. P., 1965. Seismic Refraction Studies of the Crustal Structure of the Hawaiian Archipelago, Pacific Sci., v. 19, pp. 315-319.

Gunn, R., 1943a. A Quantitative Evaluation of the
    influence of the lithosphere on the anomalies of
    gravity, J. Franklin Inst., v. 236, pp. 47-65.

_____, 1943b. A Quantitative Study of isobaric
    equilibrium and gravity anomalies in the Hawaiian
    Islands, J. Franklin Inst., v. 236, pp. 373-390.

_____, 1947. Quantitative aspects of juxtaposed
    ocean deeps, mountain chains and volcanic ranges,
    Geophysics, v. 12, pp. 238-255.

_____, 1949. Isostasy-Extended, J. Geol., v. 57,
    pp. 263-279.

Hamilton, E. L., 1970. Sound Velocity and Related Proper-
    ties of Marine Sediments, North Pacific, J. Geophys.
    Res., v. 75, pp. 4423-4446.

_____, 1971. Prediction of in-situ acoustic and elas-
    tic properties of marine sediments, Geophysics, v. 36,
    v. 36, pp. 266-284.

_____, 1973. Marine Geology of the Aleutian Abyssal
    Plain, Marine Geology, v. 14, pp. 295-325.

Hamilton, E. L., et al., 1974. Sediment Velocities from
    Sonobuoys: Bengal, Bering Sea, Japan Sea, and North
    Pacific, J. Geophys. Res., v. 79, pp. 2653-2668.

Hanks, T. C., 1971. The Kuril Trench-Hokkaido Rise
    System: Large Shallow Earthquakes and Simple models
    of Deformation, Geophys. J. R. Astr. Soc., v. 23,
    pp. 173-189.

Heiskanen, W. A., and Vening-Meinesz, F. A., 1958. The
    Earth and its Gravity Field, McGraw-Hill, 470 pp.

Hertz, H., 1884. On the equilibrium of floating elastic
    plates, Wiedemann's Annalen, v. 22, pp. 449-455.

Hetenyi, M., 1946. Beams on elastic foundation, The
    University of Michigan Press, Ann Arbor, Michigan,
    255 pp.

Hilde, T. W. C., 1976. Mesozoic Sea-Floor Spreading in
    the North Pacific, Geophys. Monograph 19, Am. Geophys.
    Union, Washington, D. C., pp. 205-226.

Houtz, R., et al., 1968. Velocity of Deep-Sea Sediments from Sonobuoy Data, J. Geophys. Res., v. 73, pp. 2615-2641.

_____, 1970. Seismic data from Sonobuoy Stations in the Northern and Equatorial Pacific, J. Geophys. Res., v. 75, pp. 5093-5111.

Houtz, R. E., and Ewing, J. I., 1963. Detailed Sedimentary Velocities from Seismic Refraction Profiles in the Western North Atlantic, J. Geophys. Res., v. 68, pp. 5233-5258.

Jeffreys, H., 1959. The Earth, 9th ed., Cambridge Univ. Press, London, 420 pp.

Kanamori, H., and Press, F., 1970. How Thick is the Lithosphere, Nature, v. 226, pp. 330-331.

Kroenke, L. W., 1965. Seismic Reflection Studies of Sediment Thickness Around the Hawaiian Ridge, Pacific Sci., v. 19, pp. 335-338.

LaCoste, L. J. B. and Harrison, J. C., 1961. Some theoretical considerations in the measurement of gravity at sea, Geophys. J. R. Astr. Soc., v. 5, pp. 89-103.

Leeds, A. R., et al., 1974. Variations of Upper Mantle Structure under the Pacific Ocean, Science, v. 186, pp. 141-143.

LePichon, X., and Talwani, M., 1964. Gravity Survey of a Seamount near 35°N and 46°W in the North Atlantic, Marine Geol., v. 2, pp. 262-277.

Love, A. E., 1944. A Treatise on the Mathematical Theory of Elasticity, fourth edition, Dover Publications, N.Y., 648 pp.

Ludwig, W. J., et al., 1968. Seismic Refraction, The Sea, v. 4, part 1, Wiley-Interscience, N. Y., pp. 53-84.

Macdonald, G. A., 1965. The Lithologic Constitution of the Crust and Mantle in the Hawaiian Area, Pacific Sci., v. 19, pp. 285-286.

Manghnani, M. G., and Woollard, G. P., 1965. Ultrasonic Velocities and Related Elastic Properties of Hawaiian Basaltic Rocks, Pacific Sci., v. 19, pp. 291-295.

Matthews, D. J., 1939. Tables of the velocity of sound in pure water and sea water for use in echo-sounding and sound-ranging, Hydrographic Dept., Admiralty, London, 52 pp.

McKenzie, D. P., 1967. Some Remarks on Heat Flow and Gravity Anomalies, J. Geophys. Res., v. 72, pp. 6261-6272.

Nadai, A., 1963. Theory of Flow and Fracture of Solids, vol. II, McGraw-Hill Book Co. Inc., N. Y., 705 pp.

Nettleton, L. L., 1939. Determination of Density for Reduction of gravimeter observations, Geophysics, v. 4, pp. 176-183.

Officer, C. B., 1974. Introduction to Theoretical Geophysics, Springer-Verlag, N. Y., 385 pp.

Parker, R. L., and Oldenburg, D. W., 1973. Thermal Model of Ocean Ridges, Nature Phys. Sci., v. 242,

Shor, G. G., Jr. 1960. Crustal Structure of the Hawaiian Ridge near Gardner Pinnacles, Bull. Seismol. Soc. of Am., v. 50, pp. 563-573.

Sleep, N. H., 1969. Sensitivity of Heat Flow and Gravity to the Mechanism of Sea-Floor Spreading, J. Geophys. Res., v. 74, pp. 542-549.

Strange, W. E., et al., 1965. An Analysis of the Gravity Field over the Hawaiian Islands in Terms of Crustal Structure, Pacific Sci., v. 19, pp. 381-389.

Talwani, M., et al., 1959. Rapid Gravity Computations for Two-Dimensional Bodies with Application to the Mendocino Submarine Fracture Zone, J. Geophys. Res., v. 64, pp. 49-59.

Timoshenko, S., 1940. Theory of Plates and Shells, first edition, McGraw-Hill Book Co. Inc., N. Y., 492 pp.

_____, 1955. Strength of Materials, third edition, D. Van Nostrand Co., Princeton, N. J., 442 pp.

Vening-Meinesz, F. A., 1929. Theory and practice of pendulum observations at sea, Waltman, Delft.

_____, 1941. Gravity over the Hawaiian Archipelago and over the Maderia Area, Proc. Netherlands Acad., Wetensia, v. 44, pp. 1-12.

Vogt, P. R., 1974. Volcano Height and Plate Thickness, Earth and Planet. Sci. Lett., v. 23, pp. 337-348.

Walcott, R. I., 1970a. Flexural Rigidity, Thickness, and Viscosity of the Lithosphere, J. Geophys. Res., v. 75, pp. 3941-3954.

_____, 1970b. Isostatic Response to loading of the crust in Canada, Can. J. Earth Science, v. 7, pp. 716-734.

_____, 1970c. Flexure of the lithosphere at Hawaii, Tectonophysics, v. 9, pp. 435-446.

_____, 1972. Gravity, flexure and the growth of sedimentary basins at a continental edge, Geol. Soc. Am. Bull., v. 83, pp. 1845-1848.

_____, 1976. Lithospheric flexure, Analysis of Gravity Anomalies, and the Propogation of Seamount Chains, Geophys. Monograph 19, Am. Geophys. Union, Washington, D. C., pp. 431-438.

Watts, A. B. and Cochran, J. R., 1974. Gravity Anomalies and Flexure of the Lithosphere along the Hawaiian-Emperor Seamount Chain, Geophys. J. R. Astr. Soc., v. 38, pp. 119-141.

_____, 1975. Gravity Effect of Downgoing Lithospheric Slabs Beneath Island Arcs, Geol. Soc. of Am. Bull., v. 86, pp. 1-4.

Watts, A. B., et al., 1975. Gravity anomalies and flexure of the lithosphere: A three dimensional study of the Great Meteor Seamount, Northeast Atlantic, J. Geophys. Res., v. 80, pp. 1391-1398.

Watts, A. B., 1976. Gravity and Bathymetry in the Central Pacific Ocean, J. Geophys. Res., v. 81, pp. 1533-1553.

Yoshii, T., 1975. Regionality of Group Velocities of Rayleigh Waves in the Pacific and Thickening of the Plate, Earth and Planet. Sci. Lett., v. 25, pp. 305-312.

Yoshii, T., et al., 1976. Thickening of the Oceanic Lithosphere, Geophys. Monograph 19, Am. Geophys. Union, Washington, D. C., pp. 423-430.